Published by Avanti Publishers

Journal of Advanced Thermal Science Research

ISSN (online): 2409-5826

Thermal Performance and Heat-mass Transfer in Ternary Hybrid Nanofluids with Straight and Corrugated Baffles: A Coupled FEM-ANN Study

Qurrat Ul-Ain[1,2], Hasan A. Abid[1,2] and Imtiaz A. Shah[1,2,*]

[1]*Department of Aerospace Engineering, King Fahd University of Petroleum and Minerals (KFUPM), Dhahran 31261, Saudi Arabia*

[2]*Interdisciplinary Research Center for Aviation and Space Exploration, King Fahd University of Petroleum & Minerals (KFUPM), Dhahran 31261, Saudi Arabia*

ARTICLE INFO

Article Type: Research Article

Academic Editor: Anju R. Gupta

Keywords:
Corrugated baffles
Heat and mass transfer
Artificial neural network
Ternary hybrid nanofluid
Thermo-solutal natural convection

Timeline:
Received: April 24, 2026
Accepted: May 26, 2026
Published: June 13, 2026

Citation: Ul-Ain Q, Abid HA, Shah IA. Thermal performance and heat-mass transfer in ternary hybrid nanofluids with straight and corrugated baffles: A coupled FEM-ANN study. J Adv Therm Sci Res. 2026; 13: 53-79.

DOI: https://doi.org/10.15377/2409-5826.2026.13.3

ABSTRACT

Background: The development of advanced thermal systems needs efficient heat and mass transfer enhancement. This research study examines thermo-solutal natural convection in a closed rectangular enclosure which contains a ternary nanofluid and two types of baffles that include straight and corrugated designs to achieve better transport performance through physical and geometric changes.

Methods: The governing two-dimensional transport equations are solved numerically using the finite element method (FEM). A comprehensive parametric analysis is performed to investigate the effects of baffle length, corrugation amplitude, number of corrugations, Rayleigh number, Lewis number and nanoparticle volume fraction. In addition, a multilayer perception based artificial neural network (ANN) is developed and trained using finite element generated data to accurately predict heat and mass transfer characteristics across varying operating conditions, providing a fast and reliable surrogate model.

Significant findings: The results reveal that corrugated baffles significantly enhance flow disturbance, thermal mixing and overall transport efficiency compared to straight baffles, leading to higher Nusselt and Sherwood numbers. Increasing the nanoparticle volume fraction from $\varphi=0$ to 0.03 increase Nusselt number from 5.6376 to 12.108 corresponding to an enhancement of approximately 114.8% while the Sherwood number increase approximately 64.8%. The ANN surrogate exhibits high predictive accuracy. In the completely held-out edge-domain test, the average Nusselt number prediction achieves R^2=0.99940, RMSE $=9.341\times10^{-3}$, and MAE $=6.366\times10^{-3}$, while the average Sherwood number prediction achieves R^2=0.99196, RMSE $=3.264\times10^{-2}$, and MAE $=2.068\times10^{-2}$. These results demonstrate the effectiveness of the coupled FEM–ANN approach for analyzing and predicting heat and mass transfer in baffled ternary-hybrid-nanofluid systems.

*Corresponding Author
Email: imtiazsha91@gmail.com
Tel: +(92) 3409170942

1. Introduction

Researchers have dedicated substantial effort to studying heat and mass transfer phenomena which occur within closed enclosures because these phenomena directly apply to engineering systems that include nuclear reactors and solar collectors and electronic device cooling systems and chemical processing units [1-4]. The enclosed spaces use natural convection as a buoyancy driven method which helps to control their internal heat distribution. Cavity design together with internal structural elements such as rods and fins and baffles which change flow patterns and boost mixing efficiency, create a substantial performance impact on these processes [5-7]. The study of enclosure geometry together with the impact of buoyancy forces and external fields, now represents the primary research area, which seeks to improve transport performance, in real world applications [8-10].

Choi [11] developed nanofluids through his method of adding nanoparticles to standard fluid materials which resulted in better thermal efficiency and improved energy flow capabilities. The research showed that using two different types of nanoparticles in hybrid nanofluid demonstrated better stability and enhanced thermal properties according to studies [12-15]. The ternary hybrid nanofluid (THNF) system combines three different types of nanoparticles with a base fluid to create advanced thermal physical properties. The research conducted by Mousavi *et al*. [16], Cakmak *et al*. [17] and Sahoo [18] proved that THNF provides better thermal performance than standard fluids and hybrid nanofluids because it has better thermal conductivity and stability and higher heat and mass transfer rates. The researchers face difficulties in finding the best particle concentration and selecting nanoparticles and developing modeling methods which restrict their complete achievement of potential.

Magneto hydrodynamics (MHD) effects together with thermo-solutal convection create extra mechanisms to control buoyancy driven flows. Magnetic fields generate Lorentz forces which interact with electrically conducting fluids to create two effects that engineers use to control thermal and solutal transport in their systems [19-22]. Thermo-solutal natural convection describes a movement process which occurs when thermal and concentration gradients create motion in various natural and industrial systems; this movement displays complex physical behavior which depends on the interaction between Rayleigh, Lewis and magnetic parameters. Multiple research studies have investigated MHD together with double diffusive convection in various closed systems; these studies explain how heat and mass transfer rates depend on different geometric designs together with varying field strengths [23-25].

The transport performance of systems depends on their geometric design and the topology of their internal surfaces. The flow patterns of corrugated or wavy surfaces and baffles create localized disturbances which generate secondary vortices and disrupt the boundary layer, resulting in higher Nusselt and Sherwood numbers than smooth or straight configurations do [11]. The research has investigated how straight baffles and wavy baffles interact with multiple applications yet studies about the combined effects of baffle corrugation and baffle length and corrugation amplitude on TSNC in enclosure filled with ternary hybrid nanofluid under MHD conditions remain insufficient.

The data driven techniques, which include artificial neural networks, have shown their worth in thermo fluid systems because they allow for the quick prediction and design optimization process after scientists train their models with high-quality simulation and experimental data [26-29]. The application of ANN-based methods has successfully predicted heat and mass transfer in nanofluids while the methods also enabled faster execution of parametric studies, which would require direct simulation in all other cases [30-33]. The research field lacks studies that combine FEM-based simulation of intricate baffled geometries with ANN models trained on ternary hybrid nanofluid datasets under MHD and double diffusive conditions.

Recent studies have further demonstrated the importance of complex enclosure geometry, nanoparticle composition, and magnetic control in improving nanofluid transport. Alipour *et al*. [34] investigated a ternary Cu-MgO-ZnO/water nanofluid in a porous cavity and highlighted the effects of magnetic field, nanoparticle shape factor, and operating parameters on thermal performance. They also considered optimization of the resulting heat-transfer response. In another study, Alipour *et al*. [35] analyzed a wavy trapezoidal porous cavity containing a water/ethylene-glycol GO-Al_2O_3 hybrid nanofluid and employed response-surface methodology to determine favorable operating conditions. Hosseinzadeh *et al*. [36] examined a MoS_2-water/ethylene-glycol mixture nanofluid in a wavy enclosure and demonstrated the usefulness of optimization methods for assessing the effects of magnetic and thermal parameters. Similarly, Hosseinzadeh *et al*. [37] investigated MHD hybrid-nanofluid convection in a wavy porous enclosure using numerical simulation together with response-surface and Taguchi optimization. Rostami *et al*. [38] analyzed magnetically influenced nanofluid convection in a porous enclosure with a complex snowflake-shaped inner wall, while Hosseinzadeh *et al*. [39, 40] examined hybrid-nanofluid transport in complex porous and wavy cavities under magnetic-field effects. These investigations confirm the significant roles of geometry, magnetic damping, porous structures, and nanoparticle characteristics in thermal transport. Nevertheless, the combined effects of straight and corrugated baffles on MHD thermo-solutal convection of Cu-CuO-Al_2O_3/H_2O ternary hybrid nanofluid, together with simultaneous prediction of heat and mass transfer behavior using an FEM-trained ANN model, remain comparatively less explored.

The study uses coupled finite element Method and artificial neural network techniques to investigate natural convection that occurs due to thermal and solutal effects in a rectangular cavity filled with Cu-Cuo-Al_2O_3/H_2O ternary nanofluid. The study systematically examines the influence of baffle length (h_f), corrugation amplitude (A), Rayleigh number (Ra), Hartmann number (Ha), corrugation number (n), nanoparticle volume fraction and Lewis number (Le) on flow topology, temperature and concentration field, and global measures of transfer responses across the investigated parameter space. The combined FEM-ANN framework provides both physical insight into the role of baffled geometries and a practical predictive tool for the design of advanced thermal systems employing ternary hybrid nanofluids.

2. Physical Model

Fig. (**1**) represent the schematic of the computational domain. The enclosure is rectangular in shape, filled with a Cu–CuO–Al_2O_3/H_2O-based ternary nanofluid. The upper wall features a centrally embedded rectangular cavity containing two wavy fins that extend vertically downward into the fluid region. The inner surface of the cavity and both wavy fins are kept at a constant high temperature ($\mathrm{T_h}$) and high concentration ($\mathrm{C_h}$), functioning as heat and mass sources. Conversely, the bottom horizontal boundary is held at a uniform lower temperature ($\mathrm{T_c}$) and concentration ($\mathrm{C_c}$). The vertical sidewalls are thermally and solutally insulated satisfying $\frac{\partial T}{\partial n} = 0$ and $\frac{\partial C}{\partial n} = 0$, while no slip conditions $u = 0$ and $v = 0$ are imposed on all solid boundaries. A uniform magnetic field of strength $\mathrm{B_0}$ is applied vertically downward, aligned with the gravitational acceleration vector g, which also acts in the negative y-direction. The fluid is assumed Newtonian, incompressible, electrically conducting and governed by the Boussinesq approximation. The flow is considered two-dimensional steady and laminar, consistent with similar

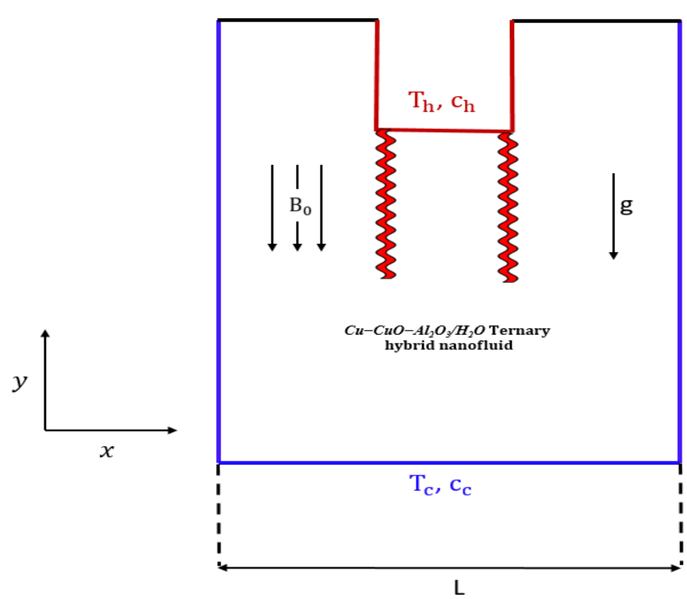

Figure 1: visual representation of the domain.

natural convection studies involving baffled and corrugated enclosures [41-44]. The steady and laminar assumption is supported by the natural convection velocity scale $U_c \sim \sqrt{g\beta_t \Delta T H}$ where $\Delta T = \mathrm{T_h} - \mathrm{T_c}$. the corresponding Reynold number is $Re_c = \frac{U_c H}{\upsilon}$ which can express as $Re_c \sim \sqrt{Ra/_{Pr}}$. Furthermore, magnetic damping increase with the Hartmann number $Ha = \mathrm{B_0} H \sqrt{\sigma/_{\mu}}$, with the Lorentz-to-viscous force ratio scaling as ${}^{F_1}/_{F\mu} \sim Ha^2$. The research examines how magnetohydrodynamics (MHD) and double-diffusive buoyancy forces and the complex wavy structure together affect heat and mass transfer. The domain exhibits horizontal symmetry while the embedded wavy fins create substantial changes to the flow pattern and temperature/concentration distribution. The geometric configuration enables researchers to study the combined effects of cavity deformation and finned structures and external magnetic fields on heat and solute transport enhancement.

3. Mathematical Formulations

3.1. Governing Equations

Under the Boussinesq approximation, the flow is assumed to be two-dimensional, steady, laminar and incompressible. The THNF is electrically conducting, while the external imposed magnetic field is uniform and directed vertically as $B = (0, -B_0, 0)$. The magnetic Rynold number is assued to be sufficient small $R_m = \mu_0 \sigma_{thnf} UL \ll 1$, so that the magnetic field induced by fluid motion is negligible compared with the imposed field. Accordingly, the quasi-static MHD approximation is adopted.

The electric current density is described by Ohms law as $J = thnf(-\nabla\psi + u \times B)$, where ψ is the electric potential. In the present two-dimension configuration, with no externally imposed electric field and no variation in the out-of-plane direction, the Lorentz force reduces to $F_1 = J \times B = \sigma_{thnf} B_0^2 u, 0,0)$. Hence the magnetic field directly damps the horizontal velocity component perpendicular to the applied magnetic field. The dimensional governing equations for conservation of mass, momentum, thermal energy and species concentration are therefore written as follow.

Continuity equation:

$$\frac{\partial \mathcal{U}}{\partial \mathcal{X}} + \frac{\partial \mathcal{V}}{\partial \mathcal{Y}} = 0 \tag{1}$$

Momentum equations:

$$\rho_{thnf}\left(\mathcal{U}\frac{\partial \mathcal{U}}{\partial \mathcal{X}} + \mathcal{V}\frac{\partial \mathcal{U}}{\partial \mathcal{Y}}\right) = -\frac{\partial \mathcal{P}}{\partial \mathcal{X}} + \mu_{thnf}\left(\frac{\partial^2 \mathcal{U}}{\partial \mathcal{X}^2} + \frac{\partial^2 \mathcal{U}}{\partial \mathcal{Y}^2}\right) + \sigma_{thnf} B_0^2 \mathcal{U} \tag{2}$$

$$\rho_{thnf}\left(\mathcal{U}\frac{\partial \mathcal{V}}{\partial \mathcal{X}} + \mathcal{V}\frac{\partial \mathcal{V}}{\partial \mathcal{Y}}\right) = -\frac{\partial \mathcal{P}}{\partial \mathcal{X}} + \mu_{thnf}\left(\frac{\partial^2 \mathcal{V}}{\partial \mathcal{X}^2} + \frac{\partial^2 \mathcal{V}}{\partial \mathcal{Y}^2}\right) + \rho_{thnf} g[\beta_T(T - T_c) + \beta_c(C - C_c)] \tag{3}$$

Energy equation:

$$\rho_{thnf} c_{p_{thnf}} \mathcal{U}\frac{\partial \mathcal{T}}{\partial \mathcal{X}} + \mathcal{V}\frac{\partial \mathcal{T}}{\partial \mathcal{Y}} = \mathcal{K}_{thnf}\left(\frac{\partial^2 \mathcal{T}}{\partial \mathcal{X}^2} + \frac{\partial^2 \mathcal{T}}{\partial \mathcal{Y}^2}\right) \tag{4}$$

Species concentration equation:

$$\mathcal{U}\frac{\partial \mathcal{C}}{\partial \mathcal{X}} + \mathcal{V}\frac{\partial \mathcal{C}}{\partial \mathcal{Y}} = \mathcal{D}_{thnf}\left(\frac{\partial^2 \mathcal{C}}{\partial \mathcal{X}^2} + \frac{\partial^2 \mathcal{C}}{\partial \mathcal{Y}^2}\right) \tag{5}$$

3.2. Thermo-Physical properties of THNF

Table **1** summarizes the thermal properties of water infused with nanoparticles such as $Cu, CuO,$ and Al_2O. The $Cu - CuO - Al_2O/H_2O$ ternary hybrid nanofluid is treated as a homogenous single-phase mixture. The total nanoparticle volume fraction is defined as $\phi = \phi_{m1} + \phi_{m2} + \phi_{m3}$ where ϕ_{m1}, ϕ_{m2} and ϕ_{m3} denotes the volume fraction of Cu, CuO, and Al_2O, respectively. The thermal properties of the base fluid and nanoparticles are listed in Table **1**, while the effective property correlations are summarized in Table **2** following Ref. [46]. The dynamic viscosity is calculated using the Brinkman-type relation while the effective thermal conductivity is obtained sequentially using the Maxwell model for the three nanoparticles components as given in Table **2**. The adopted effective-property formulation assumes uniformly dispersed, effectively spherical nanoparticle without explicit aggregation. Therefore, particle shape factor, particle size effects and aggregation are not independently resolved in the present single-phase model. Alternative property correlation may change the absolute values of Nu and Sh, consequently, the present prediction are restricted to the adopted Maxwell-Brinkman effective-property framework.

Table 1: Thermal characteristics of water and nanoparticles [45].

Physical Properties	Water (f) (Base Fluid)	Cu ($p1$)	CuO ($p2$)	Al_2O_3 ($p3$)
ρ $\left({}^{kg}/_{m^3}\right)$	997.0	8960	6310	3900
C_p $\left({}^{J}/_{kgK}\right)$	4180	385	530	880
k $\left({}^{W}/_{mK}\right)$	0.62	400	76.5	30
β $\left({}^{1}/_{K}\right)$	2.07×10^{-4}	2.1×10^{-5}	18×10^{-6}	8.5×10^{-6}
σ $(\Omega.\mathrm{m})^{-1}$	0.01	5.96×10^{7}	34.5	1×10^{-10}

Table 2: Physical properties of nanoparticles [46].

	Properties of the THNF
Nanoparticles concentration	$\phi = \phi_{m1} + \phi_{m2} + \phi_{m3}$
Density	$\rho_{hnf} = (1-\phi_{m1})\left[(1-\phi_{m2})\left[(1-\phi_{m3})\rho_f + \phi_{m3}\rho_{m3}\right] + \phi_{m2}\rho_{m2}\right] + \phi_{m1}\rho_{m1}$
Dynamic viscosity	$\mu_{thnf} = \dfrac{\mu_f}{(1-\phi_{m1})^{2.5}(1-\phi_{m2})^{2.5}(1-\phi_{m3})^{2.5}}$
Thermal conductivity	$\dfrac{\kappa_{thnf}}{\kappa_{hnf}} = \dfrac{\kappa_{m1} + 2\kappa_{hnf} - 2\phi_{m1}(\kappa_{hnf} - \kappa_{m1})}{\kappa_{m1} + 2\kappa_{hnf} + \phi_{m1}(\kappa_{hnf} - \kappa_{m1})}$ $\dfrac{\kappa_{hnf}}{\kappa_{nf}} = \dfrac{\kappa_{m2} + 2\kappa_{nf} - 2\phi_{m2}(\kappa_{nf} - \kappa_{p2})}{\kappa_{m2} + 2\kappa_{nf} + \phi_{m2}(\kappa_{nf} - \kappa_{p2})}$ $\dfrac{\kappa_{nf}}{\kappa_f} = \dfrac{\kappa_{m3} + 2\kappa_f - 2\phi_{m3}(\kappa_f - \kappa_{m3})}{\kappa_{m3} + 2\kappa_f + \phi_{m3}(\kappa_f - \kappa_{m3})}$
Heat capacity	$(\rho C_p)_{thnf} = (1-\phi_{m1})\left[(1-\phi_{m2})\left[(1-\phi_{m3})(\rho C_p)_f + \phi_{m3}(\rho C_p)_{m3}\right] + \phi_{m2}(\rho C_p)_{m2}\right] + \phi_{m1}(\rho C_p)_{m1}$
Thermal expansion	$(\rho\beta)_{thnf} = (1-\phi_{m1})\left[(1-\phi_{m2})\left[(1-\phi_{m3})(\rho\beta)_f + \phi_{m3}(\rho\beta)_{m3}\right] + \phi_{m2}(\rho\beta)_{m2}\right] + \phi_{m1}(\rho\beta)_{m1}$
Thermal diffusivity	$\alpha_{thnf} = \dfrac{\kappa_{thnf}}{(\rho C_P)_{thnf}}$
Electrical conductivity	$\dfrac{\sigma_{thnf}}{\sigma_{hnf}} = 1 + \left[\dfrac{3\left(\frac{\sigma_{m1}}{\sigma_{hnf}} - 1\right)\phi_{m1}}{\left(\frac{\sigma_{m1}}{\sigma_{hnf}} + 2\right) - \left(\frac{\sigma_{m1}}{\sigma_{hnf}} - 1\right)\phi_{m1}}\right]$ $\dfrac{\sigma_{hnf}}{\sigma_{nf}} = 1 + \left[\dfrac{3\left(\frac{\sigma_{m2}}{\sigma_{nf}} - 1\right)\phi_{m2}}{\left(\frac{\sigma_{m2}}{\sigma_{nf}} + 2\right) - \left(\frac{\sigma_{m2}}{\sigma_{nf}} - 1\right)\phi_{m2}}\right]$ $\dfrac{\sigma_{nf}}{\sigma_f} = \left[1 + \dfrac{3\left(\frac{\sigma_{m3}}{\sigma_f} - 1\right)\phi_{m3}}{\left(\frac{\sigma_{m3}}{\sigma_f} + 2\right) - \left(\frac{\sigma_{m3}}{\sigma_f} - 1\right)\phi_{m3}}\right]$

To simplify the problem, we introduce the following non-dimensional variables:

$$(\mathbb{X},\mathbb{Y})=\frac{(x,y)}{L},(\mathbb{U},\mathbb{V})=\frac{(u,v)L}{\alpha_{thnf}},\mathbb{P}=\frac{pL^2}{\rho_{thnf}\alpha_{thnf}^2},\theta=\frac{T-T_c}{T_h-T_c},\phi=\frac{C-C_c}{C_h-C_c}. \tag{6}$$

Applying the transformations, the dimensionless governing equations are:

$$\frac{\partial\mathbb{U}}{\partial\mathbb{X}}+\frac{\partial\mathbb{V}}{\partial\mathbb{Y}}=0 \tag{7}$$

$$\mathbb{U}\frac{\partial\mathbb{U}}{\partial\mathbb{X}}+\mathbb{V}\frac{\partial\mathbb{U}}{\partial\mathbb{Y}}=-\frac{\partial\mathbb{P}}{\partial\mathbb{X}}+Pr\left(\frac{\partial^2\mathbb{U}}{\partial\mathbb{X}^2}+\frac{\partial^2\mathbb{U}}{\partial\mathbb{Y}^2}\right)-PrHa^2\mathbb{U} \tag{8}$$

$$\mathbb{U}\frac{\partial\mathbb{V}}{\partial\mathbb{X}}+\mathbb{V}\frac{\partial\mathbb{V}}{\partial\mathbb{Y}}=-\frac{\partial\mathbb{P}}{\partial\mathbb{Y}}+Pr\left(\frac{\partial^2\mathbb{V}}{\partial\mathbb{X}^2}+\frac{\partial^2\mathbb{V}}{\partial\mathbb{Y}^2}\right)+Ra\,Pr\,(\theta+N\phi) \tag{9}$$

$$\mathbb{U}\frac{\partial\theta}{\partial\mathbb{X}}+\mathbb{V}\frac{\partial\theta}{\partial\mathbb{Y}}=\frac{\partial^2\theta}{\partial\mathbb{X}^2}+\frac{\partial^2\theta}{\partial\mathbb{Y}^2} \tag{10}$$

$$\mathbb{U}\frac{\partial\phi}{\partial\mathbb{X}}+\mathbb{V}\frac{\partial\phi}{\partial\mathbb{Y}}=\frac{1}{Le}\left(\frac{\partial^2\phi}{\partial\mathbb{X}^2}+\frac{\partial^2\phi}{\partial\mathbb{Y}^2}\right) \tag{11}$$

The associated dimensionless boundary conditions are:

- Top embedded cavity surface and wavy fins: $\theta=1,\phi=1$
- Along the cold surfaces: $\theta=0,\phi=0$
- For the adiabatic surfaces: $\frac{\partial\theta}{\partial n}=\frac{\partial\phi}{\partial n}=0$
- No-slip conditions (all walls): $\mathbb{U}=\mathbb{V}=0$

The attained dimensionless numbers are:

$$Pr=\frac{v_{thnf}}{\alpha_{thnf}},Ra=\frac{g\beta_T(T_h-T_c)L^3}{v_{thnf}\alpha_{thnf}},Ha=B_0L\sqrt{\frac{\sigma_{thnf}}{\mu_{thnf}}},Le=\frac{\alpha_{thnf}}{D_{thnf}},N=\frac{\beta_c(C_h-C_c)}{\beta_T(T_h-T_c)}. \tag{12}$$

The Nusselt and Sherwood numbers of the heated surfaces are expressed as

$$Nu_{local}=-\frac{k_{thnf}}{k_f}\theta_Y\Big\}_{Y=0},\text{and } Sh_{local}=-C_Y\}_{Y=0}, \tag{13}$$

$$Nu_{avg}=\int_0^1 Nu_{local}\,dX,\ \text{and } Sh_{avg}=\int_0^1 Sh_{local}\,dX. \tag{14}$$

4. Numerical Method

To solve (7-11) the coupled partial differential equations governing magnetohydrodynamic thermo-solutal convection in the complex domain shown in Fig. (**1**), the finite element method (FEM) is employed using COMSOL Multiphysics 6.3 version. This platform was selected because it offers flexibility in managing complex enclosures, such as the wavy upper cavity and embedded fins, and its robust solvers for multi-physics simulations.

4.1. Discretization Approach

The fluid domain is divided into triangular elements through the application of an unstructured mesh method. Local mesh refinement creates the mesh around upper cavity and internal wavy fins areas to achieve precise results. The governing equations are transformed into weak form and discretized element-wise to construct the global stiffness matrix. A quadratic Lagrange interpolation method applies to all field variables which include velocity components pressure temperature and concentration.

4.2. Weak Formulation

Consider $W = [H^1(\Omega)]^3$ is the test subspaces for U, V, θ and C and $Q = L^2(\Omega)$ is the test space for pressure. The governing equations, when represented in weak form, are formulated as:

$$\int_\Omega (U_X + V_X)\, q d\Omega = 0, \tag{15}$$

$$\int_\Omega (UU_X + VU_Y)\, w d\Omega + \int_\Omega P_X\, w d\Omega + \frac{\mu_{thnf}}{\rho_{thnf}\alpha_f}\int_\Omega [(U_{XX} + U_{YY})]\, w d\Omega = 0, \tag{16}$$

$$\begin{aligned}\int_\Omega (UV_X + VV_Y)\, w d\Omega + \int_\Omega P_Y\, w d\Omega + \frac{\mu_{thnf}}{\rho_{thnf}\alpha_f}\int_\Omega [(V_{XX} + V_{YY})]\, w d\Omega - \frac{(\rho\beta)_{thnf}}{\rho_{thnf}\beta_f}\, Ra\, \mathrm{Pr}\int_\Omega (\theta + NC)\, w d\Omega \\ + \frac{\sigma_{thnf}\, \rho_f}{\sigma_f \rho_{thnf}} Ha^2 Pr \int_\Omega \mathrm{V}\, w d\Omega = 0,\end{aligned} \tag{17}$$

$$\int_\Omega (U\theta_X + V\theta_Y)\, w d\Omega - \frac{\alpha_{thnf}}{\alpha_f}\int_\Omega (\theta_{XX} + \theta_{YY})\, w d\Omega = 0, \tag{18}$$

$$\int_\Omega (UC_X + VC_Y)\, w d\Omega - \frac{1}{Le}\int_\Omega (C_{XX} + C_{YY}) = 0. \tag{19}$$

In the finite dimensions sub-spaces, discrete solutions are close to continuous ones.

$$\left.\begin{array}{r} U \approx \mathrm{U}_h \in \mathcal{W}_h \\ V \approx \mathcal{V}_h \in \mathcal{W}_h \\ \theta \approx \theta_h \in \mathcal{W}_h \\ C \approx \mathcal{C}_h \in \mathcal{W}_h \\ P \approx \mathcal{P}_h \in \mathcal{Q}_h \end{array}\right\} \tag{20}$$

Eq. (20) in Eq. (15)–(19) yields the discrete version that follows:

$$\int_\Omega \left(U_{h_X} + V_X\right) q_h d\Omega = 0, \tag{21}$$

$$\int_\Omega \left(U_h U_{h_X} + V_h U_{h_Y}\right) w_h d\Omega + \int_\Omega P_{h_X}\, w_h d\Omega + \frac{\mu_{thnf}}{\rho_{thnf}\alpha_f}\int_\Omega \left[\left(U_{h_{XX}} + U_{h_{YY}}\right)\right] w_h d\Omega = 0, \tag{22}$$

$$\begin{aligned}\int_\Omega \left(U_h V_{h_X} + U_h V_{h_Y}\right) w_h d\Omega + \int_\Omega P_{h_Y}\, w_h d\Omega + \frac{\mu_{thnf}}{\rho_{thnf}\alpha_f}\int_\Omega \left[\left(V_{h_{XX}} + V_{h_{YY}}\right)\right] w_h d\Omega - \frac{(\rho\beta)_{thnf}}{\rho_{thnf}\beta_f}\, Ra\, \mathrm{Pr}\int_\Omega (\theta_h + NC)\, w_h d\Omega \\ + \frac{\sigma_{thnf}\, \rho_f}{\sigma_f \rho_{thnf}} Ha^2 Pr \int_\Omega V_h\, w_h d\Omega = 0,\end{aligned} \tag{23}$$

$$\int_\Omega \left(U_h \theta_{h_X} + V_h \theta_{h_Y}\right) w_h d\Omega - \frac{\alpha_{thnf}}{\alpha_f}\int_\Omega \left(\theta_{h_{XX}} + \theta_{h_{YY}}\right) w_h d\Omega = 0, \tag{24}$$

$$\int_\Omega \left(U_h C_{h_X} + V_h C_{h_Y}\right) w_h d\Omega - \frac{1}{Le}\int_\Omega \left(C_{h_{XX}} + C_{h_{YY}}\right) w_h d\Omega = 0. \tag{25}$$

The discrete solution is defined using basis functions.

$$U_h \approx \sum_{k=1}^{\text{ndof}} U_k \varphi_k(X,Y),$$
$$V_h \approx \sum_{k=1}^{\text{ndof}} V_k \varphi_k(X,Y),$$
$$P_h \approx \sum_{k=1}^{\text{ndof}} P_k \varphi_k(X,Y), \tag{26}$$
$$\theta_h \approx \sum_{k=1}^{\text{ndof}} \theta_k \varphi_k(X,Y),$$
$$C_h \approx \sum_{k=1}^{\text{ndof}} C_k \varphi_k(X,Y),$$

On the basis of Eqs. (21)–(25), one obtains

$$\int_\Omega \left(U_{h_X} + V_X\right) q_h d\Omega = 0, \tag{27}$$

$$\int_\Omega \left(U_h U_{h_X} + V_h U_{h_Y}\right) w_h d\Omega + \int_\Omega P_{h_X} w_h d\Omega + \frac{\mu_{thnf}}{\rho_{thnf}\alpha_f}\int_\Omega \left[\left(U_{h_X} w_{h_X} + U_{h_Y} w_{h_Y}\right)\right] w_h d\Omega = 0, \tag{28}$$

$$\begin{aligned}\int_\Omega \left(U_h V_{h_X} + U_h V_{h_Y}\right) w_h d\Omega + \int_\Omega P_{h_Y} w_h d\Omega + \frac{\mu_{thnf}}{\rho_{thnf}\alpha_f}\int_\Omega \left[\left(V_{h_X} w_{h_X} + V_{h_Y} w_{h_Y}\right)\right] w_h d\Omega \\ - \frac{(\rho\beta)_{thnf}}{\rho_{thnf}\beta_f} Ra \Pr \int_\Omega (\theta_h + NC) w_h d\Omega + \frac{\sigma_{thnf}\,\rho_f}{\sigma_f \rho_{thnf}} Ha^2 Pr \int_\Omega V_h w_h d\Omega = 0,\end{aligned} \tag{29}$$

$$\int_\Omega \left(U_h \theta_{h_X} + V_h \theta_{h_Y}\right) w_h d\Omega - \frac{\alpha_{thnf}}{\alpha_f}\int_\Omega \left(\theta_{h_X} w_{h_X} + \theta_{h_Y} w_{h_Y}\right) w_h d\Omega = 0, \tag{30}$$

$$\int_\Omega \left(U_h C_{h_X} + V_h C_{h_Y}\right) w_h d\Omega - \frac{1}{Le}\int_\Omega \left(C_{h_X} w_{h_X} + C_{h_Y} w_{h_Y}\right) w_h d\Omega = 0. \tag{31}$$

In matrix representation

$$\begin{bmatrix} \frac{\mu_{thnf}}{\rho_{thnf}\alpha_f} L_h + N(U_h, V_h) & 0 & B_1 & 0 \\ 0 & \frac{\mu_{thnf}}{\rho_{thnf}\alpha_f} L_h + N_h(U_h, V_h) & B_2 & -\frac{(\rho\beta)_{thnf}}{\rho_{thnf}\beta_f} Ra \Pr M_h - \frac{\sigma_{thnf}\,\rho_f}{\sigma_f \rho_{thnf}} Ha^2 Pr M_h \\ B_1^T & B_2^T & 0 & 0 \\ 0 & 0 & 0 & L_h + N_h(U_h, V_h) \\ & 0\ 0\ 0\ L_h + N_h(U_h, V_h) & & \end{bmatrix} \begin{bmatrix} U \\ V \\ P \\ \theta \\ C \end{bmatrix} = \begin{bmatrix} \mathcal{F}_1 \\ \mathcal{F}_2 \\ \mathcal{F}_3 \\ \mathcal{F}_4 \\ \mathcal{F}_5 \end{bmatrix},$$

This can be expressed as: Aξ = $\mathcal{F}$. The nonlinear system is solved through iterative calculations, continuing until a defined convergence condition is met. The nonlinear iterations were continued until the residual norm decreased below10^{-6}. This convergence criterion was applied consistently to all investigated parameter combinations, including cases involving strong buoyancy, magnetic damping, and thermos-solutal coupling. Convergence was accepted only after the residual criterion was satisfied and no appreciable iterative changes were observed in the dependent variables. A separate sensitivity analysis using different initial guesses, continuation paths, or tolerances tighter than 10^{-6} was not performed, therefore, the present numerical results are restricted to the adopted solver settings and investigated parameter range.

4.3. Mesh Independence and Optimal Mesh Selection

Numerical simulations that involve complex geometric designs require precise mesh strategies to ensure their accurate performance. The study includes a complete mesh sensitivity assessment to establish the optimal grid sensitivity while testing mesh independence. The unstructured triangular elements are used to create a computational domain that contains vertically embedded straight and wavy baffles in the upper heated cavity.

The analysis used four mesh cases which Fig. (**2**) shows as the base case with straight baffles and three different corrugation patterns that include 6 corrugations, 9 corrugations, and 12 corrugations. The mesh uses more refined sections to create better results for thermal and solutal gradient detection through baffles and heated walls.

The mesh convergence analysis was performed using nine progressively refined unstructured meshes. In addition to Nu_{avg} and Sh_{avg}, the average velocity magnitude, temperature and concentration were evaluated at $h_f = 0.4$ (baffles height), n=9 (baffles corrugation) w=0.8 (Baffles wavelength), Pr = 6.2, N= 1, Ha= 25, $\mathrm{Ra} = 10^4$, Le = 2.5, and φ = 0.04, to examine convergence of both the flow and scalar field. The results are summarized in Table **3**.

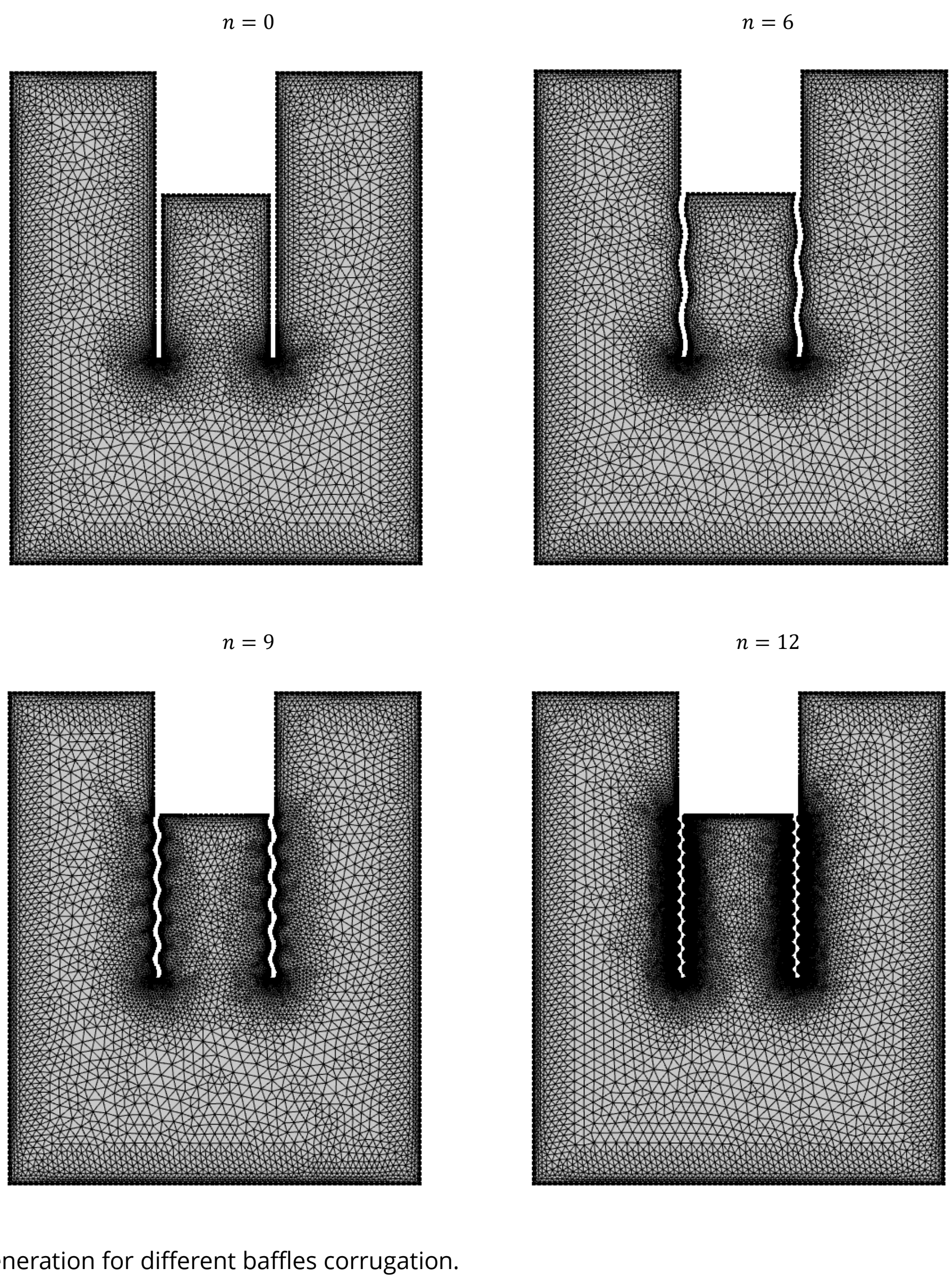

Figure 2: Mesh generation for different baffles corrugation.

Table 3: Mesh convergence assessment based on average velocity magnitude, temperature, concentration, add Nu_{avg} and Sh_{avg}.

Mesh Level	No. of Elements	DOF	Average Velocity Magnitude	Average Temperature	Average Concentration	Nu_{avg}	Sh_{avg}
M1	1314	12501	0.30499	10.445	0.26533	11.234	0.31625
M2	1862	17430	0.30473	10.347	0.26847	11.302	0.32503
M3	3238	29202	0.30461	10.235	0.26807	11.583	0.40317
M4	4952	43851	0.30450	10.157	0.26747	11.635	0.41030
M5	6287	54546	0.30444	10.120	0.26724	11.652	0.41520
M6	9270	78654	0.30435	10.094	0.26701	11.756	0.44588
M7	15199	127158	0.30426	10.065	0.26722	11.968	0.51212
M8	33097	270441	0.30415	10.045	0.26730	12.108	0.55152
M9	41837	335991	0.30413	10.040	0.26735	12.114	0.55383

The relative difference between the two finest meshes was evaluated as R. E= $\frac{|\mathrm{M9}-\mathrm{M8}|}{|\mathrm{M9}|} \times 100$. The correspondence difference were 0.0066% for average velocity magnitude, 0.0498% for average temperature, 0.0187% for average concentration, 0.0495% for Nu_{avg} and 0.4171% for Sh_{avg}. Since all variation remain below 0.5%, further mesh refinement produced negligible changes in the numerical solution. Accordingly, Mesh 8, containing 33097 elements and 270441 degrees of freedom was selected for the remaining simulation as suitable balance between computational cost and numerical accuracy.

The mesh configurations are tested with multiple n values because baffle corrugation requires testing through 0 to 12 cycle intervals. The updated mesh design in each instance enables accurate monitoring of flow patterns together with thermal and solute diffusion at the corrugated boundary areas.

4.4. Model Validation and Accuracy Evaluation

The present numerical results were validated against the experimental and numerical findings reported by Lizardi *et al*. [47]. The reference configuration was used as an independent benchmark for buoyancy-driven natural convection rather than as an exact reproduction of the present corrugated-fin, ternary hybrid nanofluid, MHD thermo-solutal system. The developed solver was first assessed at Ra = 2.705 × 10^6 and the predicted Nu_{avg} showed close agreement with the published experimental and numerical values. Specifically, the present value of Nu_{avg} = 13.87 differs by approximately 4.996% from the experimental value of 13.21 and by only 0.216% from the numerical value of 13.90, as summarized in Table **4**.

A second validation was performed by comparing the velocity profile for the case without protuberances at Ra = 2.705 × 10^6 and Pr = 6.78. As shown in Fig. (**3a**-**c**), the predicted velocity distribution closely follows the experimental and numerical profiles reported in Ref. [30]. Because the original point-by-point experimental velocity data were not available, a quantitative profile error could not be evaluated reliably. Nevertheless, the close agreement in both the velocity-profile shape and the Nu_{avg} supports the accuracy and reliability of the present numerical formulation.

Table 4: Validation of Nu_{avg} against experimental results by [47].

Nu_{avg}		
Experimental [47]	**Numerical [47]**	**Present Study**
13.21	13.90	13.87

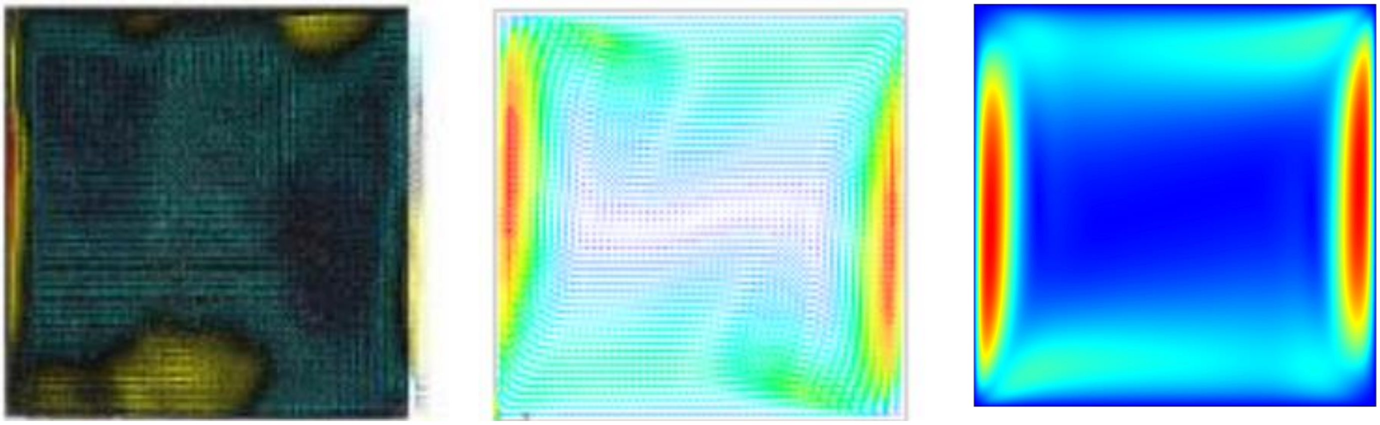

a: Velocity Profile (experimental, [47]) **b:** Velocity Profile (numerical, [47]) **c:** Velocity profile (numerical, present work)

Figure 3: Comparison of velocity profiles for the case without protuberances at Ra = 2.705 × 10^6 and Pr = 6.78.

5. Results with Discussion

This section presents a comprehensive analysis of the numerical findings for thermo-solutal convection of the $Cu + CuO + Al_2O_3/H_2O$ ternary hybrid nanofluid within the considered enclosure equipped with zigzag baffles. The impact of key dimensionless parameters, including the Rayleigh number (Ra), Hartmann number (Ha), number of baffle corrugations (n), baffles length (h_f), baffles amplitude (A), and nanoparticle volume fraction (φ), are examined in detail. The discussion emphasizes the influence of these parameters on flow structure, temperature distribution, concentration field, and heat and mass transfer rates, quantified in terms of the Nu_{avg} and Sh_{avg}. Streamlines, isotherms, and isoconcentration contours are presented to visualize the physical behavior, while quantitative trends are supported by ANN-based predictive modeling.

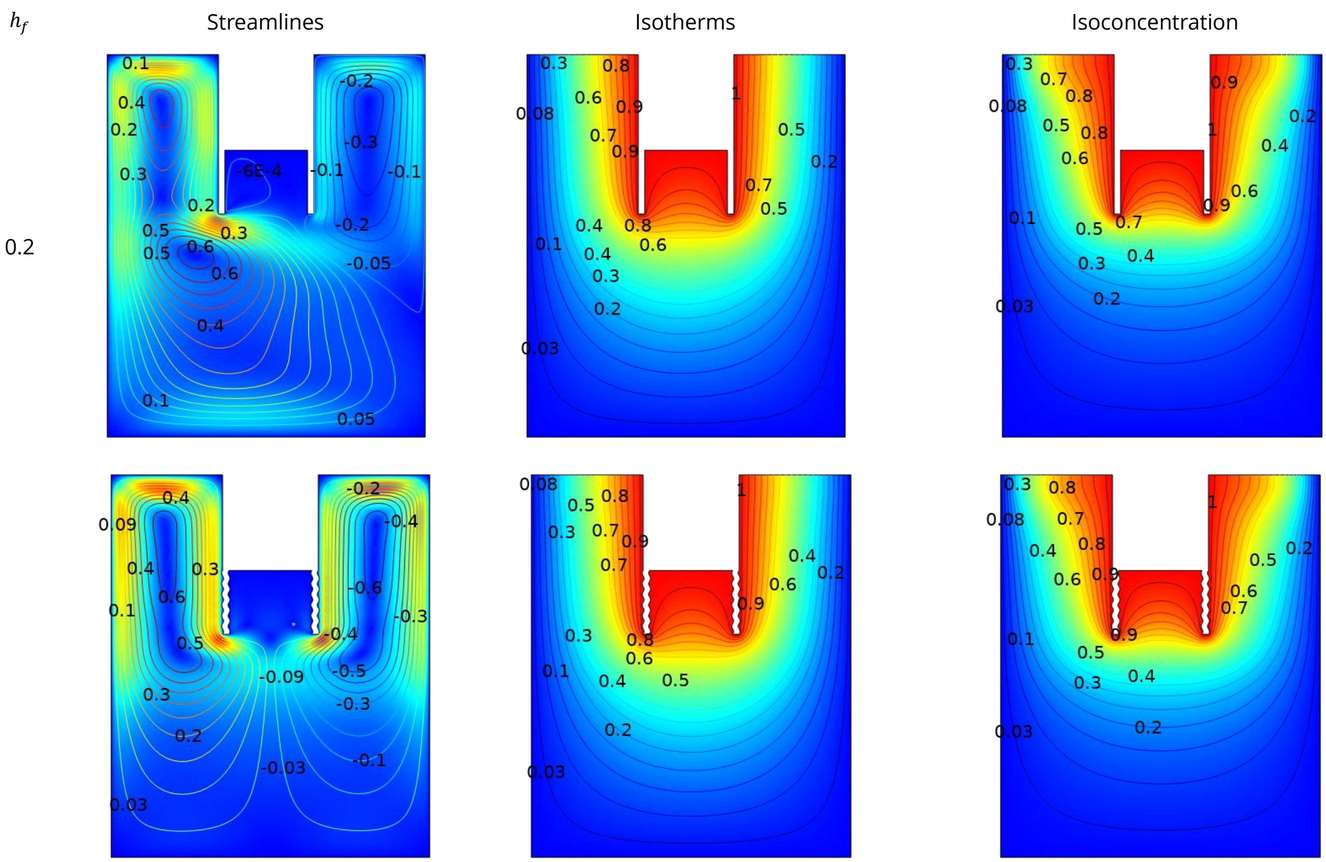

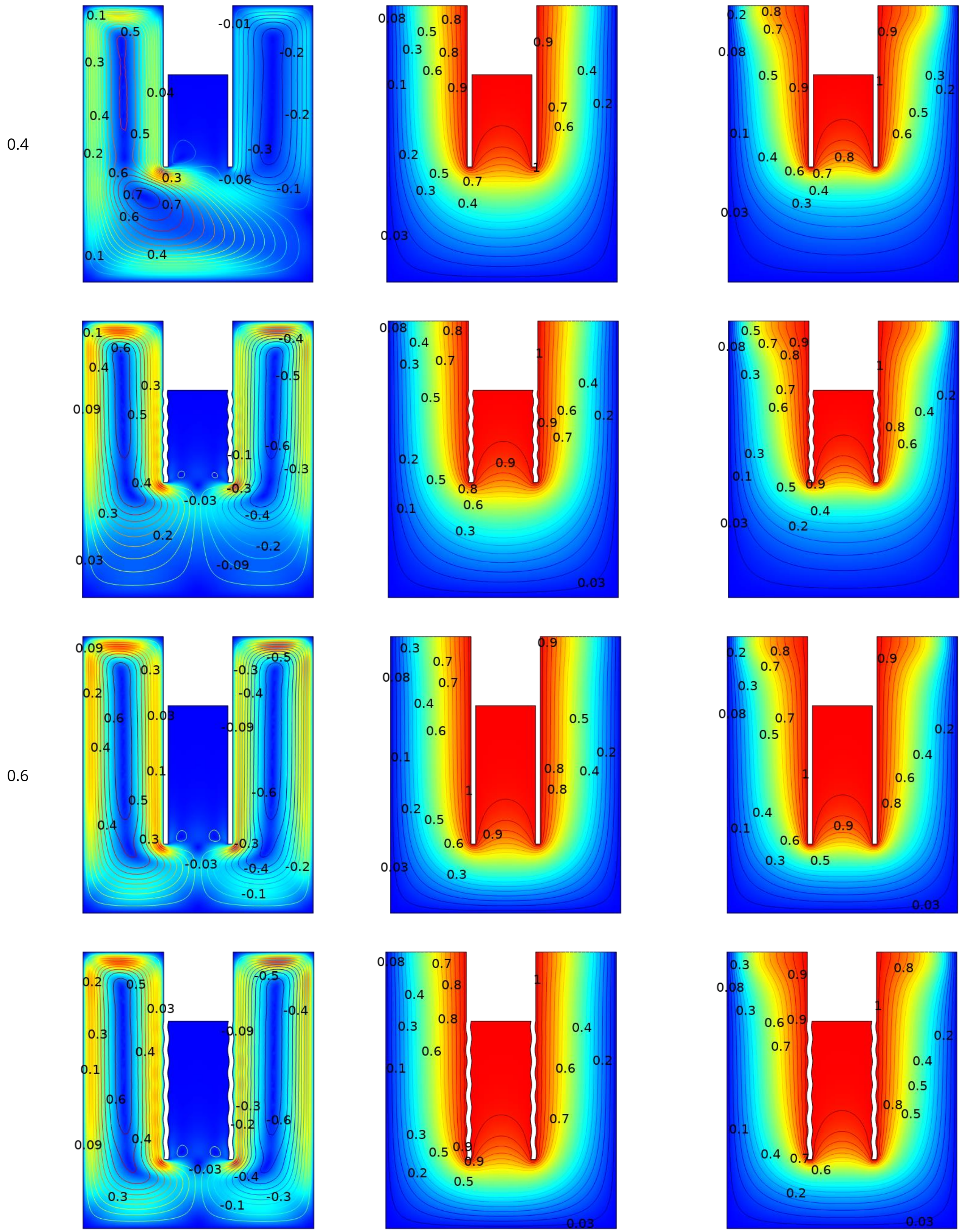

Figure 4: Variation in streamlines, temperature isotherm, and concentration fields with h_f.

Fig. (**4**) depicts the effect of baffle length (h_f =0.2, 0.4, 0.6) for straight and wavy configurations on the streamlines, isotherms, and concentration contours at fixed values of at $n = 6$, Pr = 6.2, N= 1, Ha= 25, $\mathrm{Ra} = 10^4$, Le = 2.5, A= 0.012, and φ = 0.04. For $h_f = 0.2$, the short baffles cause minimal obstruction to the main circulation cell, resulting in a large, well-developed primary vortex spanning most of the cavity. The thermal and concentration gradients maintain their vertical orientation because both straight and wavy configurations produce minimal changes to the diffusion layers. The baffles start to penetrate the flow domain when h_f reaches 0.4, which causes the primary vortex to break into smaller secondary recirculation that form near the baffle tips. The wavy configuration creates localized mixing zones through its undulating surface, which enhances thermal dispersion better than the straight baffle. Baffles at $h_f = 0.6$ occupy most of the enclosure height, which limits the main vortex movement while producing numerous small recirculation cells. The straight configuration causes the air to become thermally stratified because it keeps hot and cold air separate in distinct areas. The wavy baffle disrupts these layers through its design, which creates cross-stream mixing while it helps distribute temperature and concentration fields throughout the entire system. The concentration contours confirm that, longer baffles which increase the confinement of the solute near its source, cause the wavy profile to improve horizontal dispersion through boundary layer disruption. Increasing h_f creates stronger obstruction effects which lead to smaller vortex sizes and different heat and mass transfer patterns, while wavy baffles demonstrate better mixing and distribution capabilities than straight ones throughout all tested lengths.

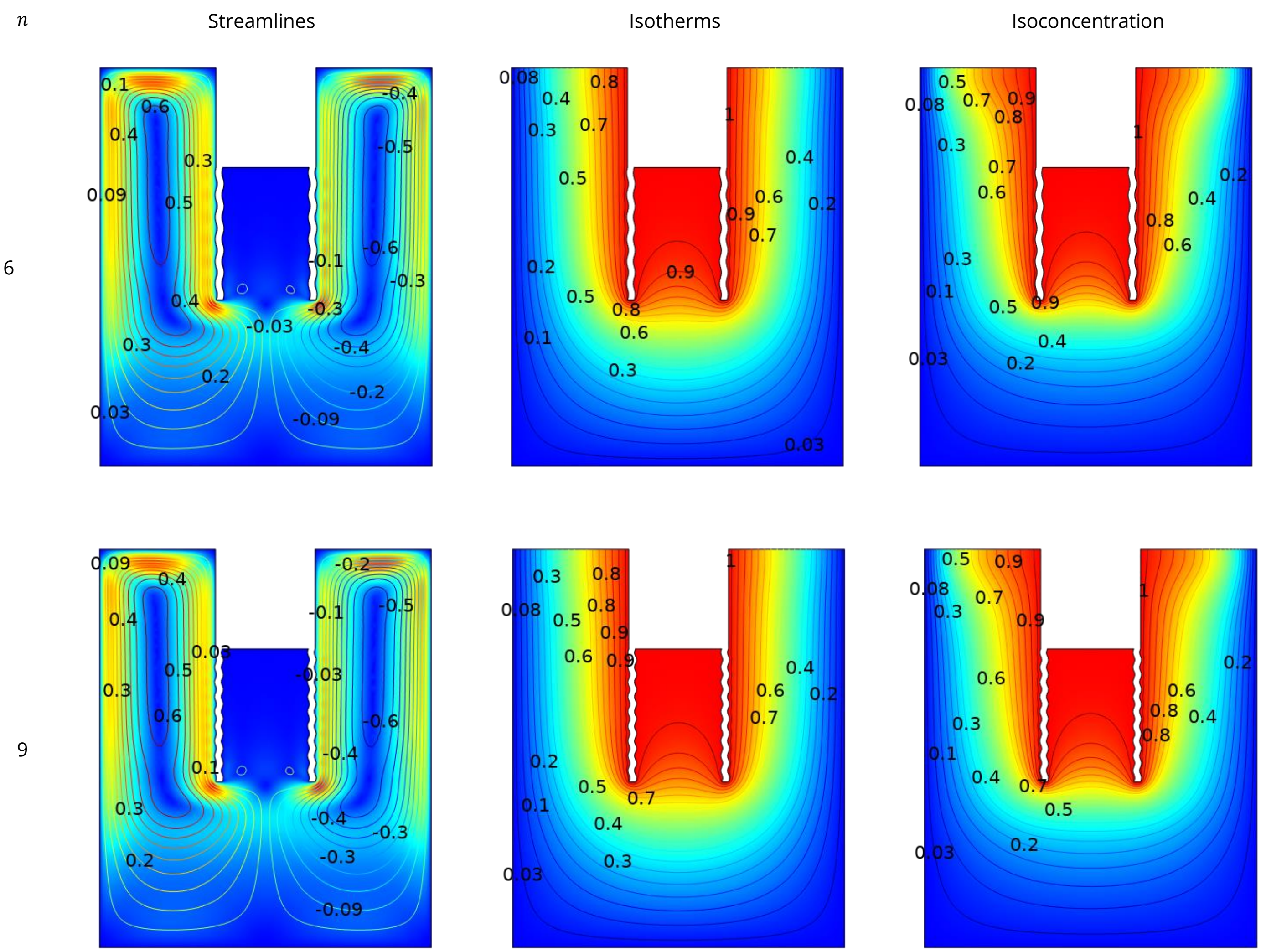

12

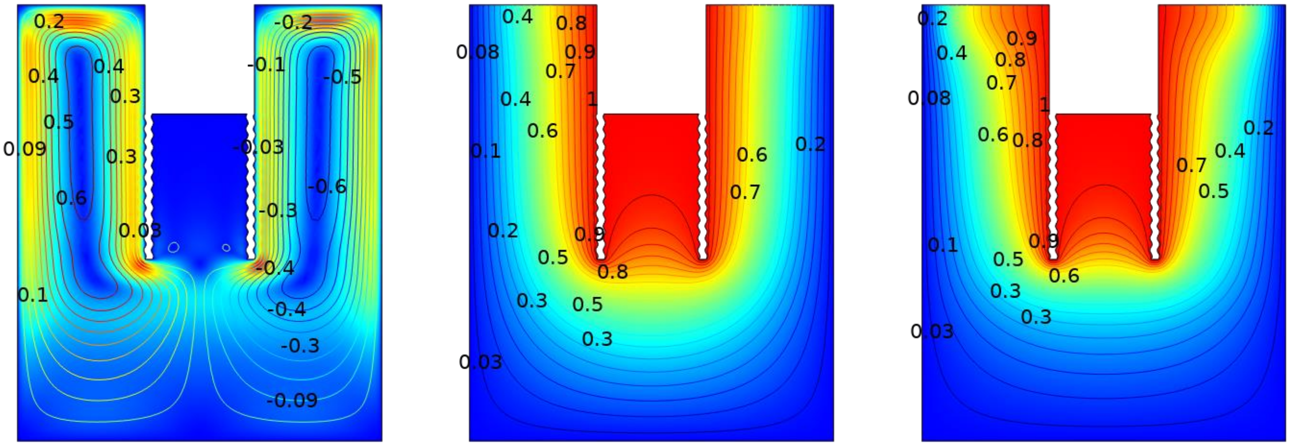

Figure 5: Variation in streamlines, temperature isotherm, and concentration fields with n.

Fig. (**5**) illustrates the impact of varying the number of baffle corrugations (n=6, 9, 12) on the streamlines, isotherm and concentration contours. The baffle interface experiences moderate flow disturbances because the surface undulations at $n = 6$ create gentle flow paths. The streamlines exhibit a main vortex pattern which shows only minor changes near the baffle surface while the isotherms maintain their parallel alignment with the heated boundaries to show only small improvements in lateral heat transfer. The baffle surface reaches its maximum curvature at 9 which creates new areas of localized recirculation that develop next to each corrugation peak and trough. The disturbances create a more wavy isotherm pattern because they disrupt the thermal boundary layers which results in stronger fluid mixing between hot and cold regions. The main flow and the corrugated surface interact more closely which causes temperature distribution to extend throughout the cavity. The increased corrugation density at $n = 12$ leads to stronger periodic flow disruptions in the flow system. The streamlines display multiple small vortical structures that occupy the entire baffle length, which shows that the system generates stronger shear-layer development and deeper surface flow connections. The isotherms show serious distortion which leads to thermal plumes being redirected across the entire area. The excessive number of corrugations increases flow resistance, which results in a small reduction of the main circulation system's power. The boundary layer disruption and thermal mixing increase as n grows, with $n = 9$ and $n = 12$ showing the most effective heat distribution improvements over $n = 6$.

A Streamlines Isotherms Isoconcentration

0.009

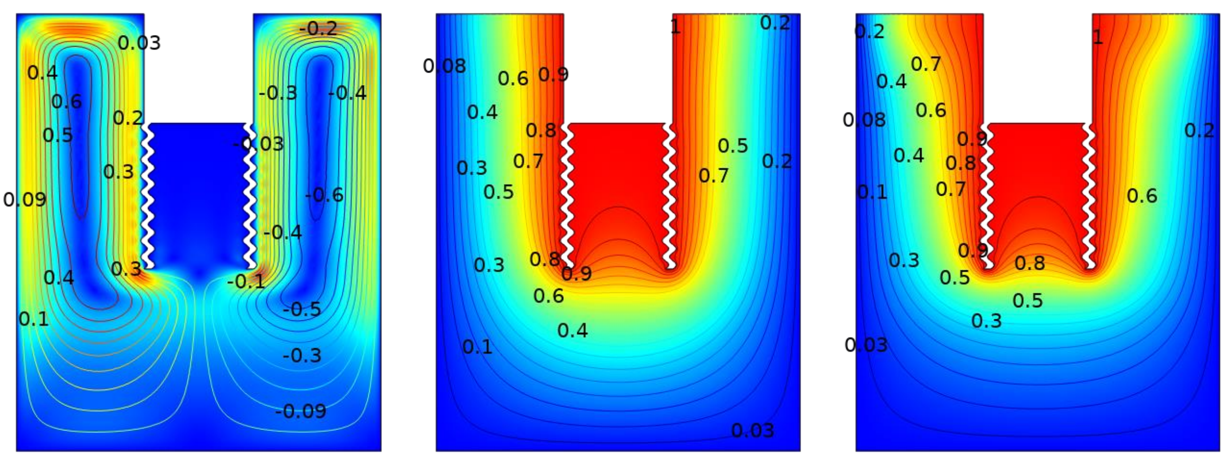

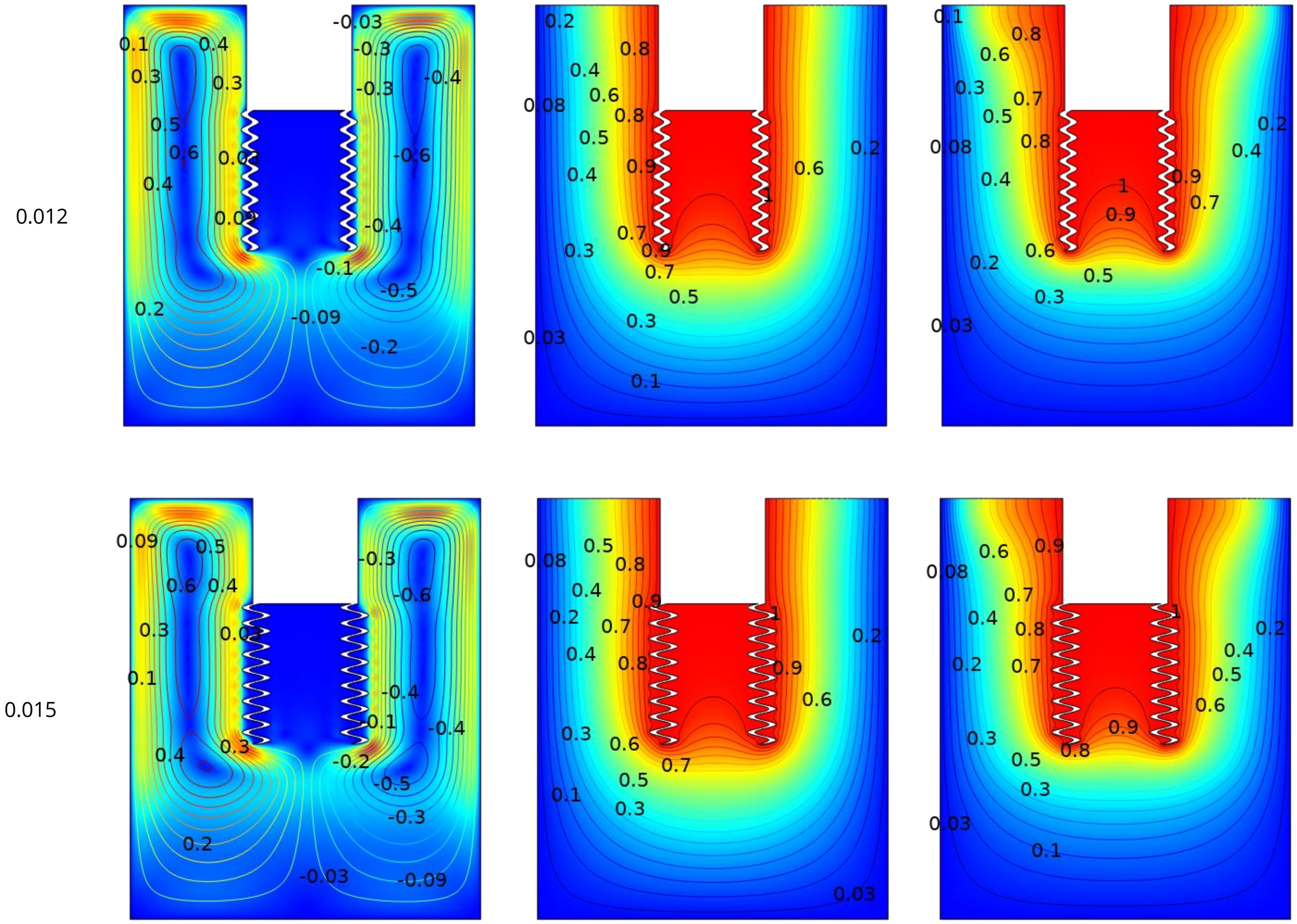

Figure 6: Variation in streamlines, temperature isotherm, and concentration fields with A.

Fig. (**6**) depicts the influence of corrugation amplitude (A=0.009, 0.012, 0.015) on the streamlines and isotherm contours. Baffle surface $A = 0.009$ shows shallow undulations which create only minor flow disturbances because of this small amplitude. The primary vortex dominates the streamlines which show a smooth circulation path while the isotherms follow the heated surfaces which limits their lateral heat distribution. The flow interacts with the baffle surface because the amplitude increases to $A = 0.012$. The deeper corrugations create localized recirculations that occur within each trough which breaks the thermal boundary layers while redistributing heat more efficiently. The isotherms show noticeable distortions which display increased thermal energy penetration into the central region of the cavity. The pronounced $A = 0.015$ corrugation depth causes flow separation to occur at the baffle which generates multiple small vortical structures and increased mixing zones. The isotherms show strong undulations because hot fluid moves deeper into the core region while cold fluid moves towards the heated walls. The increased surface complexity enhances thermal uniformity but it creates additional resistance against main circulation which results in a minor decrease of primary vortex strength.

Fig. (**7**) presents the effect of Ra $(10^3, 10^4, 10^5)$ on the streamlines, isotherm and isoconcentration distribution. The lowest value of Ra (10^3) shows that conduction serves as the primary heat transfer mechanism which leads to only minimal buoyancy-induced movement of fluids. The streamlines show a primary vortex which moves in a slow manner and the isotherms maintain almost straight lines which stay at regular intervals between the heated and cooled surfaces to demonstrate minimal airflow patterns that cause distortion. The Ra value increase to 10^5 leads to stronger buoyancy effects which enhance the main circulation pattern while creating secondary flow patterns that emerge from the baffle tips and corrugations. The heated regions show isotherms which start to bend and tighten together because convection creates a more effective movement of heat from the hot areas to the colder areas. The dominant heat transfer mechanism at 10^6 reaches its peak when convection takes control of all heat transfer. The streamlines show strong main circulation movements which create small areas of reverse flow because of the baffle design that uses corrugated patterns. The isotherms display strong deformation patterns which show rapid thermal shifts above the heated surfaces and extensive thermal distribution throughout the center of the cavity.

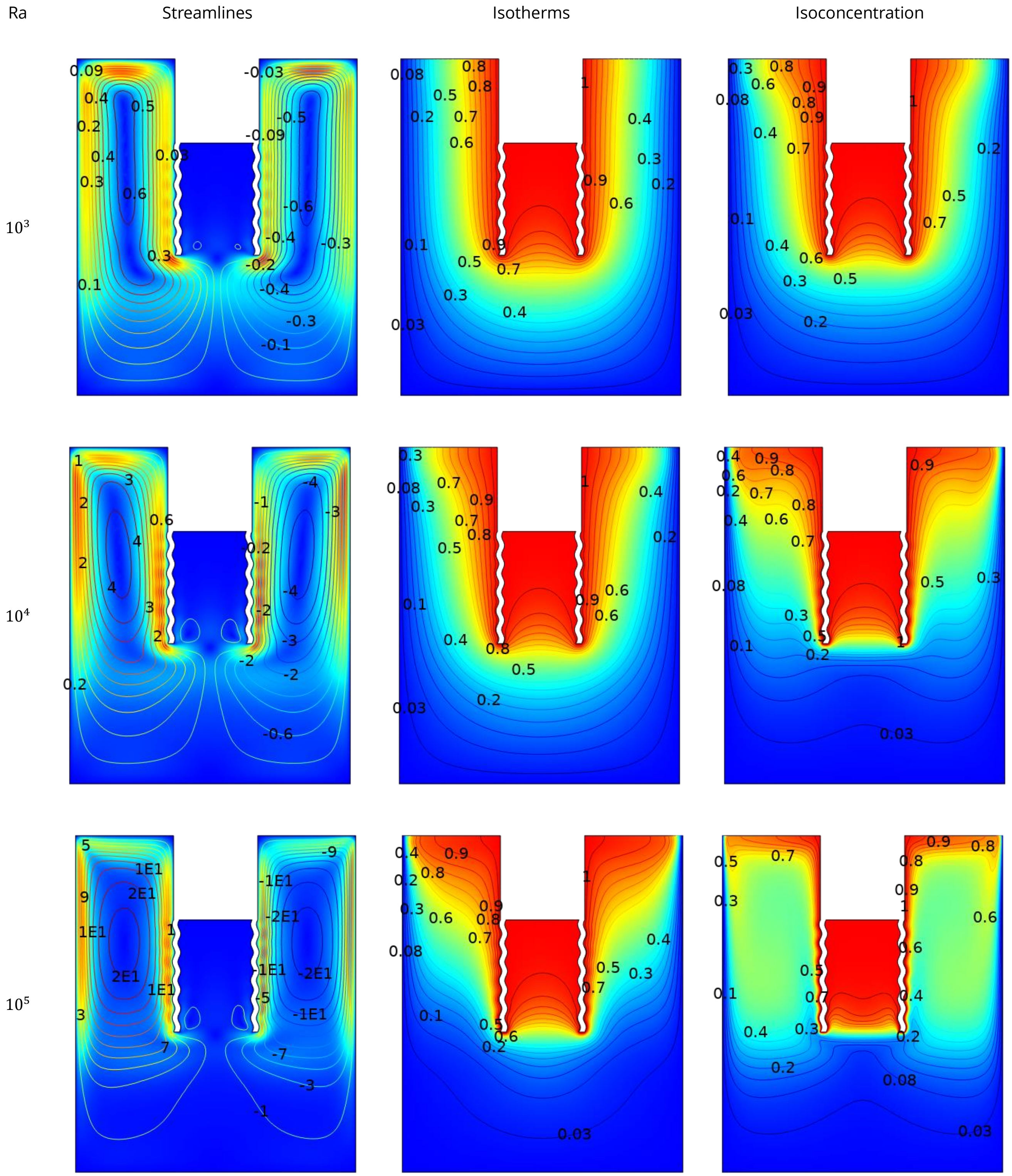

Figure 7: Variation in streamlines, temperature isotherm, and concentration fields with Ra.

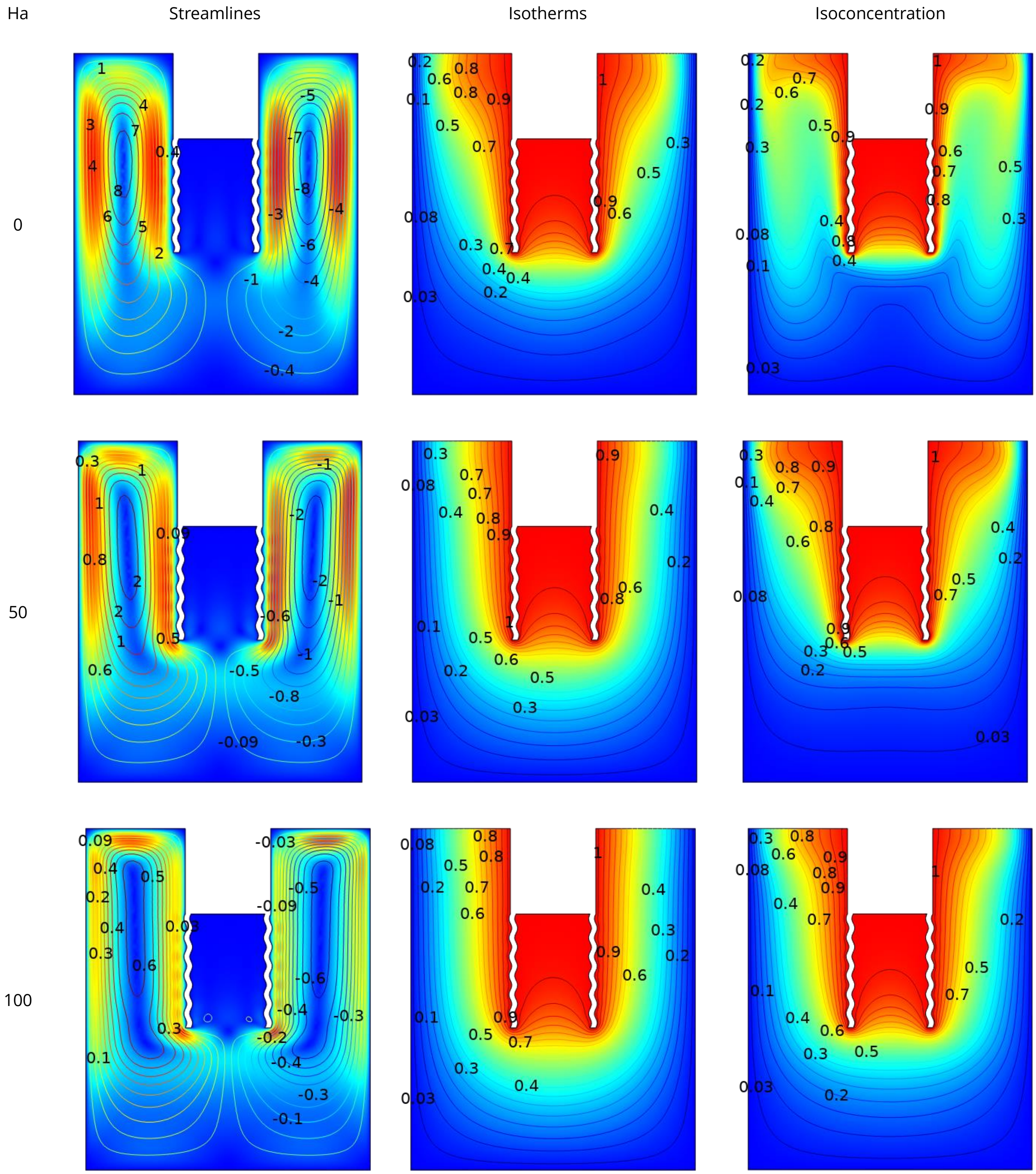

Figure 8: Variation in streamlines, temperature isotherm, and concentration fields with Ha.

Fig. (**8**) shows the influence of Ha (Ha=0, 50, 100) on the streamlines, isotherm and concentration contours. The system with no magnetic field active at $Ha = 0$ shows buoyancy forces as the dominant force which creates strong airflow patterns that move through the cavity space. The streamlines show one main vortex which generates multiple small recirculation cells through the baffle system's corrugated design. The isotherms show clear distortion patterns which demonstrate effective convection-based heat distribution. The magnetic field at $Ha = 50$ induces Lorentz forces which produce a damping effect on fluid movement that results in decreased velocity and smaller primary vortex strength. The isotherm suppression decreases isotherm distortion while creating a thermal field which shows more distinct temperature layers because convection continues to occur. The magnetic damping effect becomes stronger at $Ha = 100$ which results in a major drop of primary circulation power and a reduction of secondary vortex size and quantity. The isotherms start to align on a horizontal plane because the fluid movement has been reduced, which creates a state where conduction becomes the main thermal transfer method. The heat transfer process now depends entirely on diffusion because the flow between hot and cold areas has been minimized. The increased Ha value creates a reduction of buoyancy-driven convection because the Lorentz force impacts, while the high Ha value results in better heat distribution but less efficient distribution.

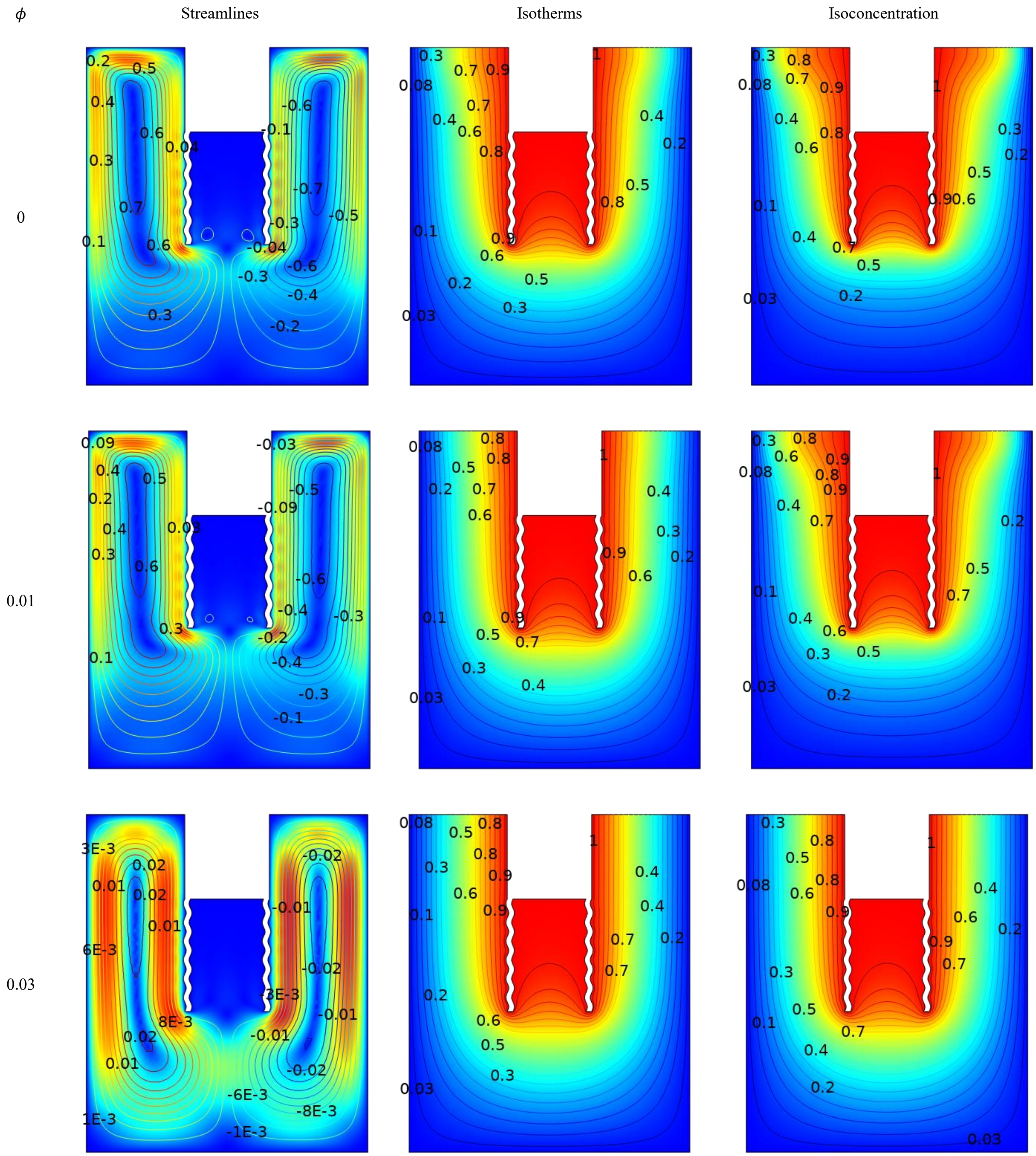

Figure 9: Variation in streamlines, temperature isotherm, and concentration fields with ϕ.

Fig. (**9**) illustrates the effect of nanoparticle volume fraction (φ=0.01, 0.02, 0.03) on the streamlines and isotherm contours. The addition of nanoparticles to base fluid at φ=0.01 results in only a slight increase of thermal conductivity which keeps the viscosity at low levels. The primary and secondary vortices form clearly visible patterns in the streamlines while the isotherms show clear distortion patterns that demonstrate efficient convective heat movement. The fluid's thermal conductivity increases when the volume fraction reaches φ=0.02 because this change enables better heat distribution throughout the cavity area. The flow structures maintain their strength while the isotherms display steeper gradients close to the heated areas to show better heat transfer performance. The thermal conductivity at φ=0.03 promotes heat distribution throughout the system but the viscosity increase that comes with it results in a minor reduction of circulation strength. The streamlines show a slight decrease in vortex strength while the isotherms maintain consistent thermal distribution which shows that thermal conductivity increase has a stronger effect than viscous damping in the tested range. The rising φ values improve heat transport because they increase effective thermal conductivity but excessive nanoparticle addition results in lower natural convection strength because fluid viscosity rises.

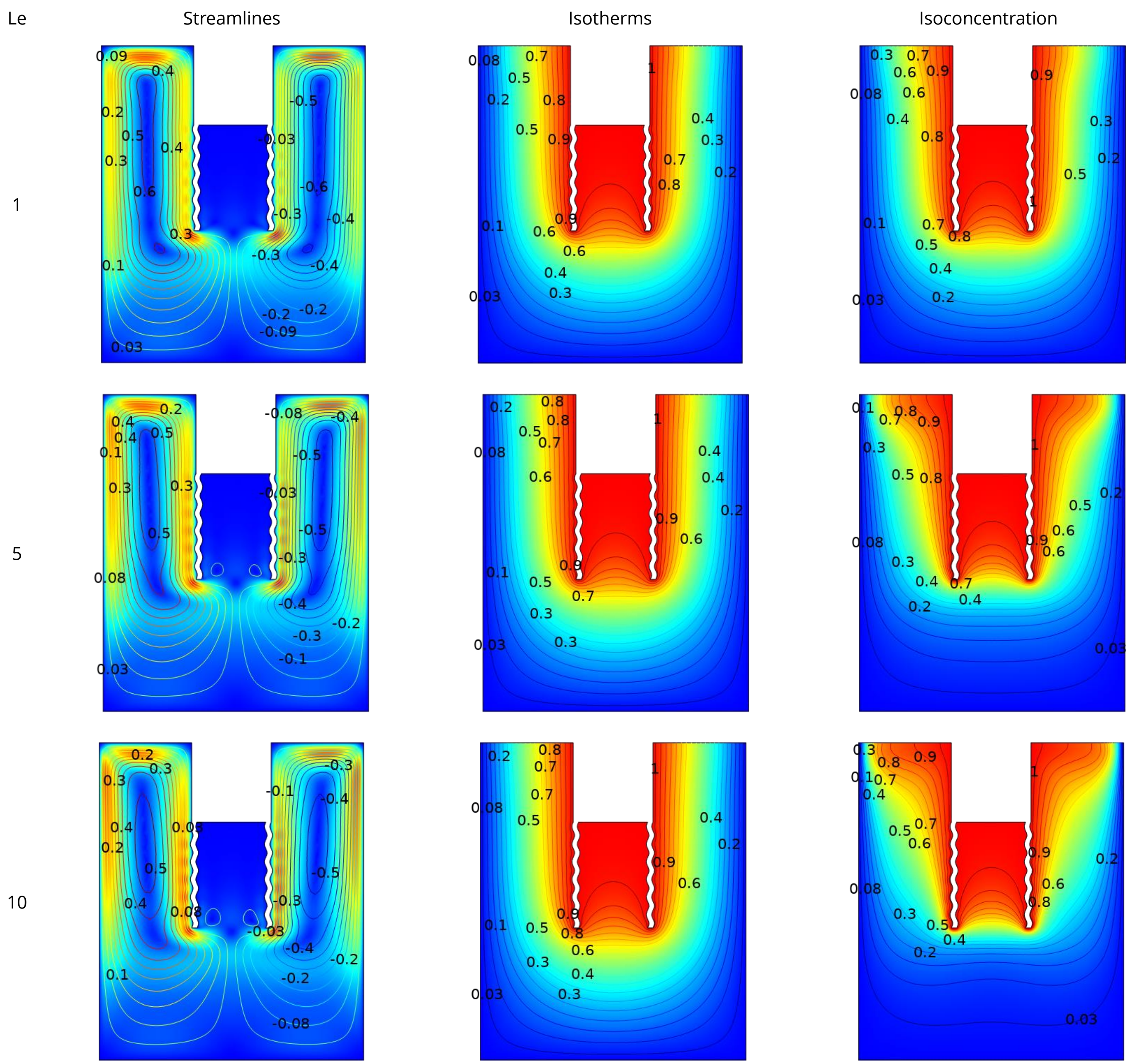

Figure 10: Variation in streamlines, temperature isotherm, and concentration fields with Le.

Fig. (**10**) presents the influence of Lewis number (Le=1, 5, 10) on the streamlines, isotherms, and concentration contours. At $Le = 1$ the thermal diffusivity moves at a faster rate than the mass diffusivity which causes temperature distribution to reach equilibrium throughout the cavity while concentration gradients stay concentrated in specific areas. The streamlines display active circulation patterns while both the isotherm lines and concentration distribution lines experience major changes because heat and substance movement through convection processes. When Le is increased to 5 the mass diffusivity decreases relative to thermal diffusivity which results in concentration fields that become more restricted while the temperature fields remain evenly distributed. The flow structure remains stable throughout the process which causes concentration contours to move closer to their source points because solutal mixing has decreased. At $Le = 10$ the mass diffusivity becomes much smaller than thermal diffusivity which causes concentration gradients to stay concentrated near their source points. The streamlines maintain their original structure but their ability to distribute the solutal field decreases. The isotherms maintain a broad distribution while the concentration contours are tightly packed which shows that species transport remains constrained.

Table 5: Variation of Nu_{avg} and Sh_{avg} for different parameters.

h_f	h_{wf}	n	A	Ra	Ha	φ	Le	Nu_{avg}	Sh_{avg}
0.2	0.4	9	0.012	10^4	100	0.01	5	9.4307	3.2536
0.4								11.169	1.6157
0.6								15.283	0.66670
0.4	0.2	9	0.012	10^4	100	0.01	5	9.4367	0.66266
	0.4							12.107	0.56823
	0.6							15.286	0.61019
0.4	0.4	3	0.012	10^4	100	0.01	5	12.095	0.57424
		6						12.105	0.56823
		9						12.107	0.57190
		12						12.114	0.57666
0.4	0.4	9	0.003	10^4	100	0.01	5	12.105	0.57190
			0.006					12.175	0.59130
			0.009					12.219	0.62611
			0.012					12.351	0.72159
0.4	0.4	9	0.012	10^4	100	0.01	5	12.108	0.55152
				10^5				13.422	1.4081
				10^6				28.049	2.5185
0.4	0.4	9	0.012	10^4	0	0.01	5	14.794	1.1546
					50			12.293	0.85306
					100			12.108	0.55152
0.4	0.4	9	0.012	10^4	100	0	5	5.6376	0.36908
						0.03		12.108	0.60828
						0.06		20.401	0.60828
0.4	0.4	9	0.012	10^4	100	0.01	1	12.111	0.43485
							5	12.105	0.73645
							10	12.101	1.0182

Table **5** presents the Nu_{avg} and Sh_{avg} across different values of h_f, n, Ra, Ha, A, Le and φ. The findings indicate that Nu_{avg} increases notably with higher $Ra, n, A,$ and φ driven by strong convective effects and improved disruption of the thermal boundary layer. Highest Nu_{avg} values are observed at Ra=10^6, n=12, A=0.015, and φ=0.06. In contrast, increasing the Ha suppresses convective flow due to the influence of Lorentz forces, leading to a decline in Nu_{avg}. A comparable pattern is seen for Sh_{avg}, which rises under intensified convection but decreases with higher Le values as reduce mass diffusivity limits solute transport. The influence of nanoparticle loading results from competing changes in thermal conductivity, viscosity, buoyancy and species diffusion. Increasing φ from 0 to 0.03 raises Nu_{avg} from 5.6376 to 12.108, corresponding to an enhancement of approximately114.8%. while Sh_{avg} increases 64.8% approximately. A further increase to φ=0.06 raises Nu_{avg} to 20.401, representing an additional increase of approximately 68.5%, whereas Sh_{avg} remains nearly unchanged at 0.60828. The continued increase in Nu_{avg} is primarily associated with the higher effective thermal conductivity, which directly increases heat conduction and wall heat flux. In contrast, the simultaneous increase in viscosity introduces additional viscous resistance and weakens the convective contribution. Because the investigated nanoparticle concentrations remain relatively low, this viscosity penalty does not dominate the thermal-conductivity benefit for heat transfer. However, the saturation of Sh_{avg} at higher φ indicates that the increased viscosity and changes in species diffusivity increasingly offset further improvement in solutal convection. Therefore, the nanoparticle effect should be interpreted as a balance between enhanced thermal conduction and increasing hydrodynamic and diffusive resistance rather than as a purely convection-driven enhancement. Moreover, the wavy baffle design consistently outperforms the straight configuration across all tested parameters, as it induces stronger flow disturbances that enhance both Nu_{avg} and Sh_{avg}.

6. Designing Artificial Neural Networks for Modeling

Artificial Neural Networks (ANNs) function as computational systems which create non-linear processing capabilities based on the operational structure of human brain systems. The system serves scientific research purposes because it enables researchers to classify data and identify patterns and make predictions through its ability to replicate human cognitive functions which include learning and forecasting [48-50]. ANN training or learning process requires network parameters to be adjusted until the system achieves maximum accuracy in predicting target outputs. The research study selects feed-forward multilayer neural network (MNN) architecture because it maintains mathematical representation as an acyclic directed graph that connects multiple processing layers. The network increases its ability to predict new input data through multiple training cycles which enable it to adjust its weights and biases.

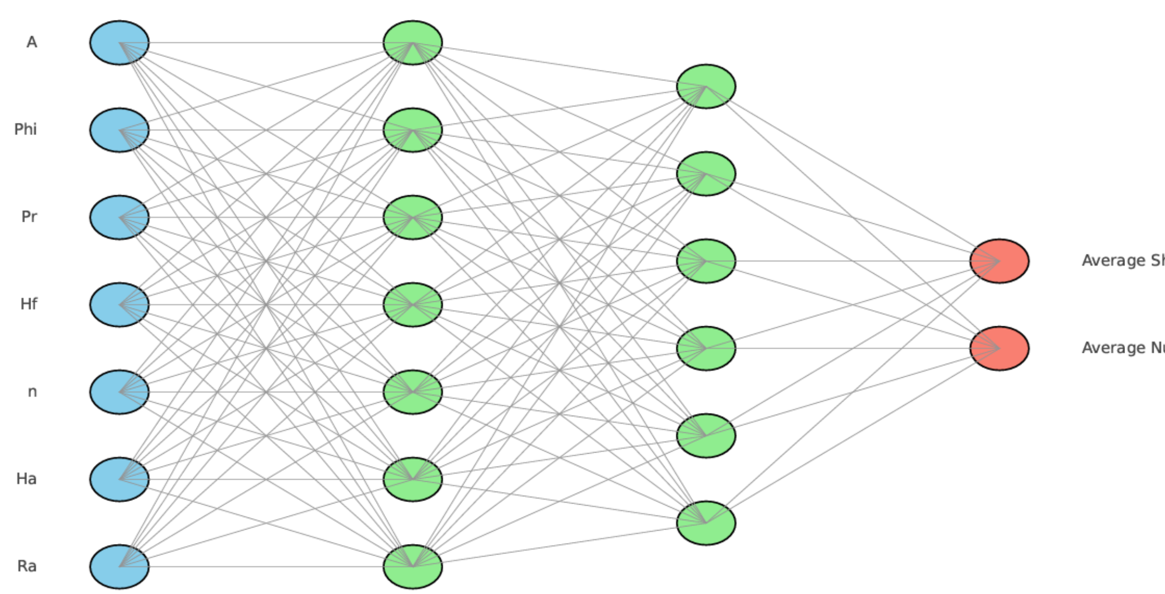

Figure 11: Structural layout of an ANN.

The ANN architecture developed in this research study contains three main components which include the input layer and hidden layer and output layer according to the description in Fig. (**11**). The input layer is composed of neurons representing the governing parameters. The output layer consists of two neurons corresponding to the predicted Nu_{avg} and Sh_{avg}. The ANN database was generated from the FEM simulations covering the investigated combinations of $h_f = 0.4$, n=9 w=0.8, Pr = 6.2, N= 1, Ha= 25, $\mathrm{Ra} = 10^4$, Le = 2.5, and φ = 0.04. The complete data set was divided into 85 % training, 10% testing, and 5% validation. To minimize information leakage, the partitioning was performed at the level of parametric groups rather than by randomly assigning neighboring individual FEM samples. Cases belonging to the same parameter family were retained within a single subset whenever possible. The training data were used to update the network weights and biases, the validation data were used to monitor generalization and prevent overfitting and the test data were kept independent and used only for final performance evaluation.

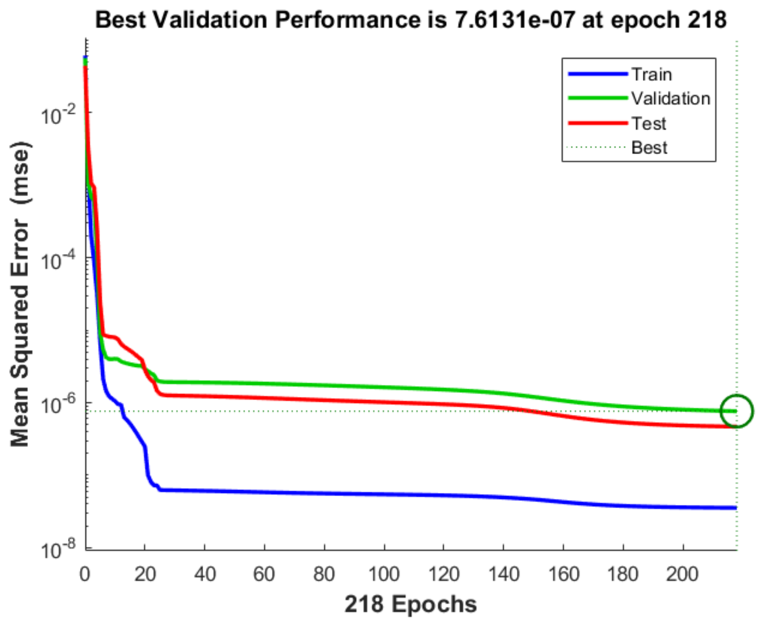

Figure 12: Epoch-wise MSE trends for training,validation and testing sets.

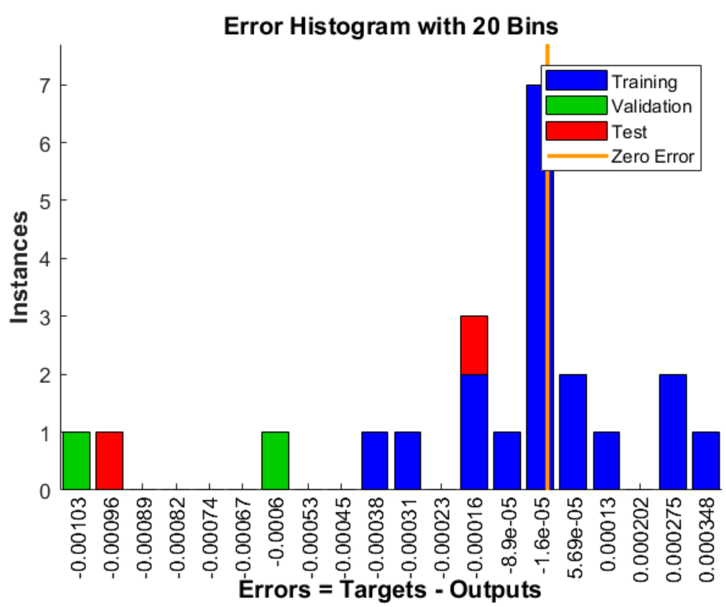

Figure 13: Distribution of errors obtained from the proposed BRT-ANN model.

The system uses a hidden layer that contains 10 neurons according to its current configuration. The MSE metric calculates the average squared difference between predicted values and actual target values, which shows prediction accuracy because reduced MSE values deliver better performance. The MSE value of zero indicates perfect model alignment with actual results. Fig. (**12**) shows the training process through multiple epochs which display MSE results for training and testing data. The best validation performance (8.3919×10^{-8}) occurred at epoch 33 according to the results. The system stops training at this stage because validation errors start to rise which leads to overfitting problems.

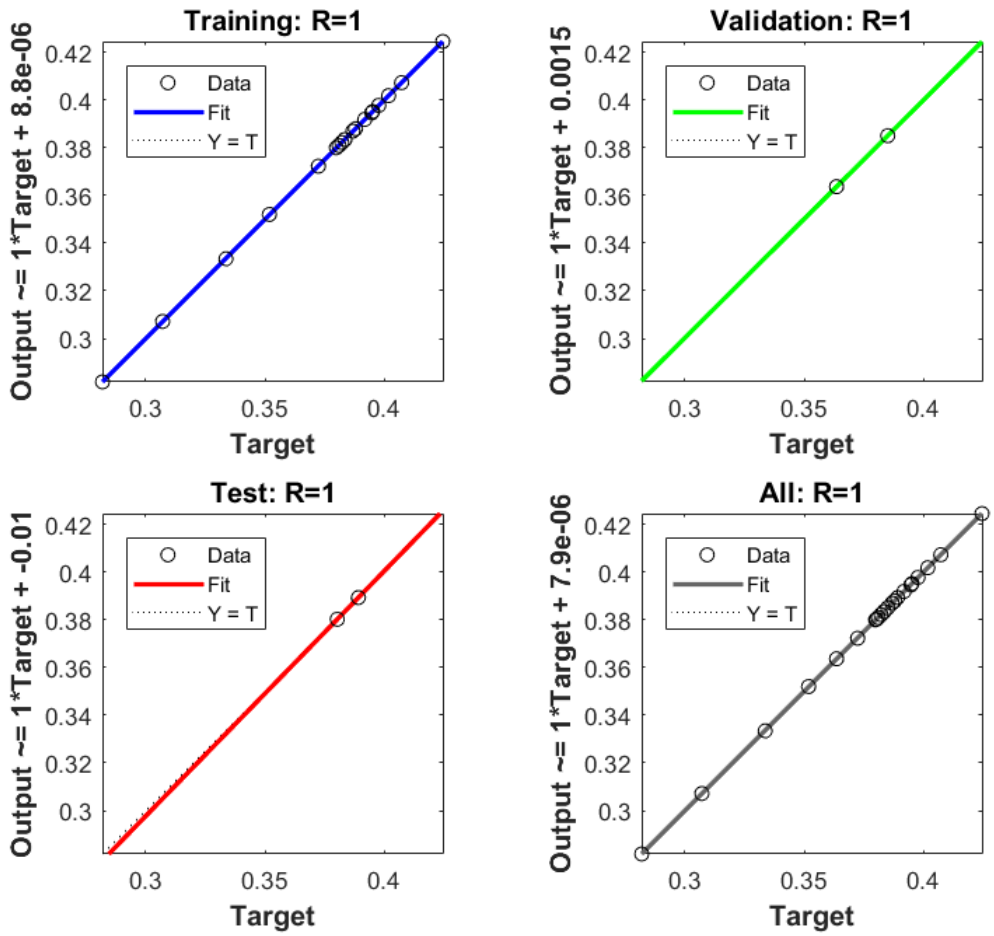

Figure 14: Rregression plot for the BRT-ANN model.

The error distribution which Fig. (**13**) displays shows that most prediction errors occur near zero which proves that the model generates consistent and impartial predictions. The regression analysis in Fig. (**14**) further confirms the network's accuracy because all datasets show regression lines that closely follow the 45° reference line while correlation coefficients approach unity to demonstrate excellent agreement between predicted and target values.

Fig. (**15**) evaluate the generalization capability of the ANN using completely held-out samples located at the lower and upper edges of the investigated Ra domain. The FEM and ANN profiles show close agreement for both Nu_{avg} and Sh_{avg}, as illustrated in Fig. (**15a**) and (**15c**). For the held-out Nusselt number data, the ANN achieves $R^2 = 0.99940$, $RMSE = 9.341\times10^{-3}$ and $MAE = 6.366\times10^{-3}$, demonstrating excellent predictive accuracy at the domain boundaries. For the Sherwood number, the corresponding values are $R^2 = 0.99196$, $RMSE = 3.264\times10^{-2}$ and $MAE = 2.068\times10^{-2}$. Although slightly larger deviation is observed in the Sherwood number, particularly near the lower Ra boundary, the prediction remains in good agreement with the FEM results. These finding demonstrate that the ANN maintain reliable predictive performance for unseen edge domain sample and exhibits limited deterioration in accuracy near the boundaries of the investigated parameter range.

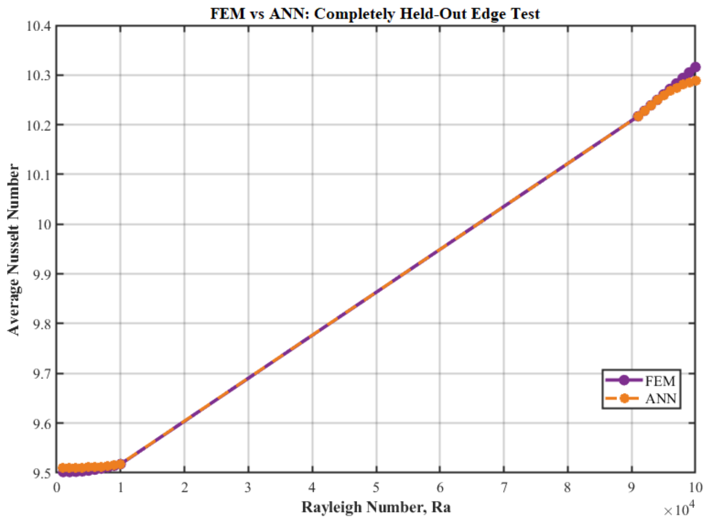

(**a**): FEM and ANN predictions of the Nu_{avg} over the Ra range.

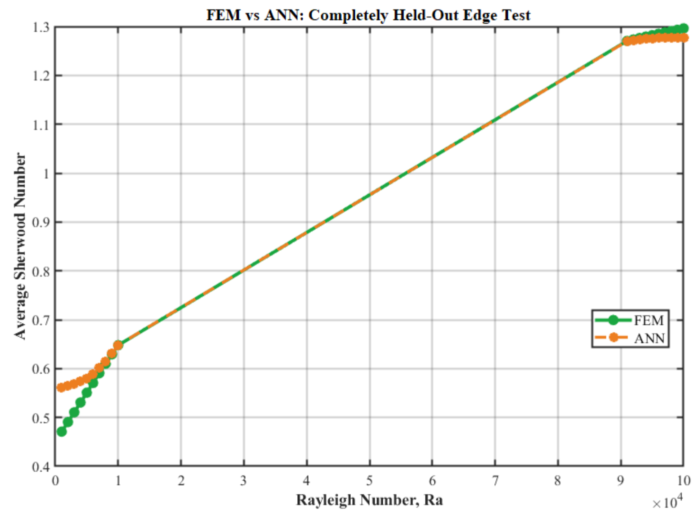

(**c**): FEM and ANN predictions of the Sh_{avg} over the Ra range.

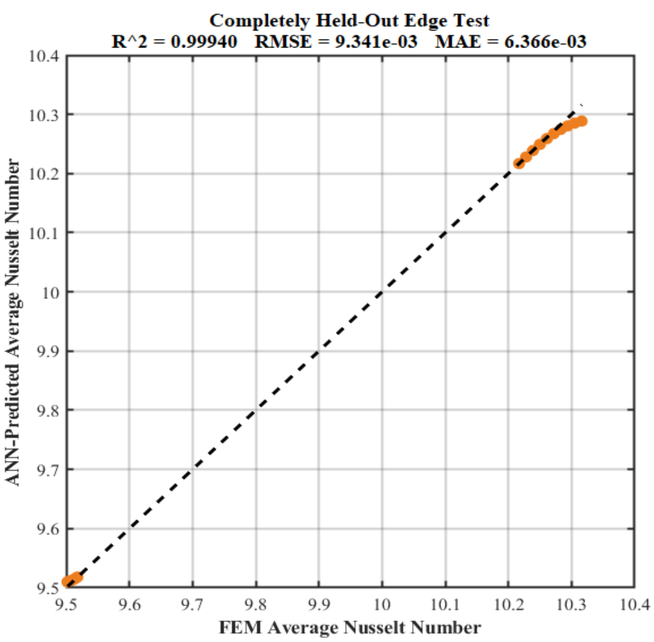

(**b**): completely held-out edge test for the Nu_{avg}.

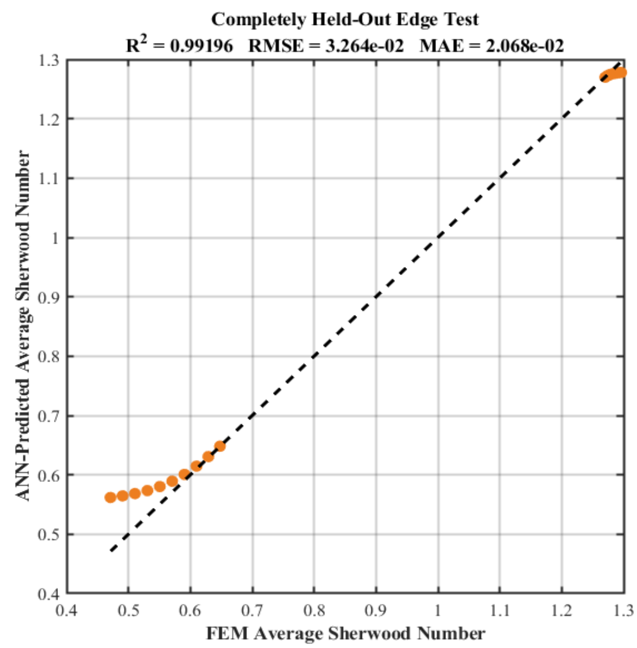

(**d**): completely held-out edge test for the Sh_{avg}.

Figure 15: External edge-domain validation of the ANN model.

7. Conclusion

The research presents a comprehensive numerical study that uses artificial neural network (ANN) methods to analyze thermo-solutal convection in a closed rectangular enclosure which contains ternary nanofluids and different baffle and corrugation designs. The findings demonstrate that increasing Rayleigh number leads to better heat and mass transfer performance, while higher Hartmann number results in diminished convective flow because of the Lorentz force effects. The mixing of flow depends on the geometric changes which include baffle length and corrugation height as essential factors. Wavy (corrugated) baffles demonstrate better performance than straight baffle designs because they produce higher Nusselt and Sherwood number results.

Furthermore, the nanoparticle volume fraction emerges as a key controlling parameter, moderate concentrations improve thermal conductivity and overall transport efficiency, while excessive loading slightly weakens fluid circulation. The ANN model demonstrates excellent predictive capability, closely matching FEM results with near-unity correlation coefficients. This conform its reliability in accurately estimating heat and mass transfer behavior across a wide range of operating conditions. Overall, the integrated FEM-ANN approach highlights the superior performance of corrugated baffles in enhancing thermo-solutal transport, offering valuable insights for the design and optimization of advanced thermal systems.

Conflicts of Interest

The authors disclose that they have no competing interests.

Funding

The study received no financial support.

Acknowledgments

Authors greatly appreciate the resources provided by the King Fahd University of Petroleum and minerals (KFUPM).

Data Availability

The data that support the findings of this study are available from the corresponding author upon reasonable request.

References

[1] Polezhaev VI, Myakshina MN, Nikitin SA. Heat transfer due to buoyancy-driven convective interaction in enclosures: Fundamentals and applications. Int J Heat Mass Transf. 2012; 55(1-3): 156-65. https://doi.org/10.1016/j.ijheatmasstransfer.2011.08.051

[2] Rahimi A, Saee AD, Kasaeipoor A, Malekshah EH. A comprehensive review on natural convection flow and heat transfer: The most practical geometries for engineering applications. Int J Numer Methods Heat Fluid Flow. 2019; 29(3): 834-77. https://doi.org/10.1108/HFF-06-2018-0272

[3] Ostrach S. Natural convection in enclosures. J Heat Transf. 1988; 110(4B): 1175-90. https://doi.org/10.1115/1.3250619

[4] Liang X, Zhang H, Tian ZF. A fourth-order compact difference algorithm for numerical solution of natural convection in an inclined square enclosure. Numer Heat Transf A Appl. 2021; 80(6): 255-90. https://doi.org/10.1080/10407782.2021.1940065

[5] Safdari Shadloo M. Application of support vector machines for accurate prediction of convection heat transfer coefficient of nanofluids through circular pipes. Int J Numer Methods Heat Fluid Flow. 2021; 31(8): 2660-79. https://doi.org/10.1108/HFF-09-2020-0555

[6] Biswas N, Mondal MK, Mandal DK, Manna NK, Gorla RSR, Chamkha AJ. A narrative loom of hybrid nanofluid-filled wavy walled tilted porous enclosure imposing a partially active magnetic field. Int J Mech Sci. 2022; 217: 107028. https://doi.org/10.1016/j.ijmecsci.2021.107028

[7] Mandal DK, Biswas N, Manna NK, Gorla RSR, Chamkha AJ. Magneto-hydrothermal performance of hybrid nanofluid flow through a non-Darcian porous complex wavy enclosure. Eur Phys J Spec Top. 2022; 231(13): 2695-712. https://doi.org/10.1140/epjs/s11734-022-00595-6

[8] Das PK, Mahmud S. Numerical investigation of natural convection inside a wavy enclosure. Int J Therm Sci. 2003; 42(4): 397-406. https://doi.org/10.1016/S1290-0729(02)00040-6

[9] Kashani S, Ranjbar AA, Mastiani M, Mirzaei H. Entropy generation and natural convection of nanoparticle-water mixture (nanofluid) near water density inversion in an enclosure with various patterns of vertical wavy walls. Appl Math Comput. 2014; 226: 180-93. https://doi.org/10.1016/j.amc.2013.10.054

[10] Mahmud S, Islam AKMS. Laminar free convection and entropy generation inside an inclined wavy enclosure. Int J Therm Sci. 2003; 42(11): 1003-12. https://doi.org/10.1016/S1290-0729(03)00076-0

[11] Choi SUS, Eastman JA. Enhancing thermal conductivity of fluids with nanoparticles. ASME International Mechanical Engineering Congress and Exposition. 1995. https://doi.org/10.1115/IMECE1995-0926

[12] Qayyum S, Hayat T, Alsaedi A. Optimization of entropy generation in motion of magnetite-Fe3O4 nanoparticles due to curved stretching sheet of variable thickness. Int J Numer Methods Heat Fluid Flow. 2019; 29(9): 3347-65. https://doi.org/10.1108/HFF-12-2018-0782

[13] Bibi A, Xu H, Sun Q, Pop I, Zhao Q. Free convection of a hybrid nanofluid past a vertical plate embedded in a porous medium with anisotropic permeability. Int J Numer Methods Heat Fluid Flow. 2020; 30(8): 4083-101. https://doi.org/10.1108/HFF-10-2019-0799

[14] Roşca NC, Roşca AV, Pop I. Axisymmetric flow of hybrid nanofluid due to a permeable non-linearly stretching/shrinking sheet with radiation effect. Int J Numer Methods Heat Fluid Flow. 2021; 31(7): 2330-46. https://doi.org/10.1108/HFF-09-2020-0574

[15] Thirumalaisamy K, Ramachandran S, Prasad VR, Bég OA, Leung HH, Kamalov F, Vajravelu K. Comparative heat transfer analysis of γ-Al2O3–C2H6O2 and γ-Al2O3–H2O electroconductive nanofluids in a saturated porous square cavity with Joule dissipation and heat source/sink effects. Phys Fluids. 2022; 34(7): 072001. https://doi.org/10.1063/5.0095334

[16] Mousavi SM, Esmaeilzadeh F, Wang XP. Effects of temperature and particles volume concentration on the thermophysical properties and the rheological behavior of CuO/MgO/TiO2 aqueous ternary hybrid nanofluid: Experimental investigation. J Therm Anal Calorim. 2019; 137(3): 879-901. https://doi.org/10.1007/s10973-019-08006-0

[17] Cakmak NK, Said Z, Sundar LS, Ali ZM, Tiwari AK. Preparation, characterization, stability, and thermal conductivity of rGO-Fe3O4-TiO2 hybrid nanofluid: An experimental study. Powder Technol. 2020; 372: 235-45. https://doi.org/10.1016/j.powtec.2020.06.012

[18] Sahoo RR. Heat transfer and second law characteristics of radiator with dissimilar shape nanoparticle-based ternary hybrid nanofluid. J Therm Anal Calorim. 2021; 146(2): 827-39. https://doi.org/10.1007/s10973-020-10039-9

[19] Rahman MM, Saidur R, Rahim NA. Conjugated effect of Joule heating and magneto-hydrodynamic on double-diffusive mixed convection in a horizontal channel with an open cavity. Int J Heat Mass Transf. 2011; 54(15-16): 3201-13. https://doi.org/10.1016/j.ijheatmasstransfer.2011.04.010

[20] Bilal S, Shah IA, Pan K, Jamshed W, Alruwaili AS, Eid MR. Investigation of thermosolutal diffusion in corrugated domain saturated with magnetized non-Newtonian fluid by performing FEM simulation. Int J Model Simul. 2025; 1-16. https://doi.org/10.1080/02286203.2025.2563980

[21] Bilal S, Shah IA, Alqahtani AS, Malik MY. Significance of aspect ratio of internal heating element in optimizing thermal production of water with ternary nano composition in crown chamber. Case Stud Therm Eng. 2025; 68: 105882. https://doi.org/10.1016/j.csite.2025.105882

[22] Mahapatra TR, Saha BC, Pal D. Magnetohydrodynamic double-diffusive natural convection for nanofluid within a trapezoidal enclosure. Comput Appl Math. 2018; 37(5): 6132-51. https://doi.org/10.1007/s40314-018-0676-5

[23] Huppert HE, Turner JS. Double-diffusive convection. J Fluid Mech. 1981; 106: 299-329. https://doi.org/10.1017/S0022112081001614

[24] Shah IA, Bilal S, Muhammad T, Eldin SM. Computational assessment about hydrothermal attributes with induction of MWNT's-Fe3O4 in water saturated in hexagonal enclosure. Case Stud Therm Eng. 2023; 47: 103036. https://doi.org/10.1016/j.csite.2023.103036

[25] Shah IA, Bilal S, Akgül A, Tekin MT, Botmart T, Zahran HY, *et al*. On analysis of magnetized viscous fluid flow in permeable channel with single wall carbon nano tubes dispersion by executing nano-layer approach. Alex Eng J. 2022; 61(12): 11737-51. https://doi.org/10.1016/j.aej.2022.05.037

[26] Uddin MB, Rahman MM, Khan MAH. Hydromagnetic double-diffusive unsteady mixed convection in a trapezoidal enclosure due to uniform and nonuniform heating at the bottom side. Numer Heat Transf A Appl. 2015; 68(2): 205-24. https://doi.org/10.1080/10407782.2014.977129

[27] Shahzad H, Ain QU, Pasha AA, Irshad K, Shah IA, Ghaffari A, *et al*. Double-diffusive natural convection energy transfer in magnetically influenced Casson fluid flow in trapezoidal enclosure with fillets. Int Commun Heat Mass Transf. 2022; 137: 106236. https://doi.org/10.1016/j.icheatmasstransfer.2022.106236

[28] Seo YM, Pandey S, Lee HU, Choi C, Park YG, Ha MY. Prediction of heat transfer distribution induced by the variation in vertical location of circular cylinder on Rayleigh-Bénard convection using artificial neural network. Int J Mech Sci. 2021; 209: 106701. https://doi.org/10.1016/j.ijmecsci.2021.106701

[29] Kalogirou SA. Applications of artificial neural-networks for energy systems. Appl Energy. 2000; 67(1-2): 17-35. https://doi.org/10.1016/S0306-2619(00)00005-2

[30] Tizakast Y, Kaddiri M, Lamsaadi M, Makayssi T. Machine learning based algorithms for modeling natural convection fluid flow and heat and mass transfer in rectangular cavities filled with non-Newtonian fluids. Eng Appl Artif Intell. 2023; 119: 105750. https://doi.org/10.1016/j.engappai.2022.105750

[31] Santhosh N, Sivaraj R, Prasad VR, Bég OA, Leung HH, Kamalov F, Kuharat S. Computational study of MHD mixed convective flow of Cu/Al2O3-water nanofluid in a porous rectangular cavity with slits, viscous heating, Joule dissipation and heat source/sink effects. Waves Random Complex Media. 2026; 36(2): 2241-74. https://doi.org/10.1080/17455030.2023.2168786

[32] Ain QU, Shah IA, Alzahrani SM. Enhanced heat transfer in novel star-shaped enclosure with hybrid nanofluids: A neural network-assisted study. Case Stud Therm Eng. 2024; 61: 105065. https://doi.org/10.1016/j.csite.2024.105065

[33] Alzahrani SM, Alzahrani TA, Shah IA. Neural network prediction of MHD thermo-solutal natural convection in ternary hybrid nanofluids within a curved enclosure. Results Phys. 2025; 73: 108275. https://doi.org/10.1016/j.rinp.2025.108275

[34] Alipour N, Jafari B, Hosseinzadeh K. Thermal analysis and optimization approach for ternary nanofluid flow in a novel porous cavity by considering nanoparticle shape factor. Heliyon. 2023; 9(12): e22257. https://doi.org/10.1016/j.heliyon.2023.e22257

[35] Alipour N, Jafari B, Hosseinzadeh K. Optimization of wavy trapezoidal porous cavity containing mixture hybrid nanofluid (water/ethylene glycol GO–Al2O3) by response surface method. Sci Rep. 2023; 13: 1635. https://doi.org/10.1038/s41598-023-28916-2

[36] Hosseinzadeh K, Akbari S, Faghiri S, Shafii MB. Optimization approach for MoS2-water ethylene glycol mixture nanofluid flow in a wavy enclosure. Int J Thermofluids. 2023; 18: 100337. https://doi.org/10.1016/j.ijft.2023.100337

[37] Hosseinzadeh K, Erfani Moghaddam MA, Nateghi SK, Shafii MB, Ganji DD. Radiation and convection heat transfer optimization with MHD analysis of a hybrid nanofluid within a wavy porous enclosure. J Magn Magn Mater. 2023; 566: 170328. https://doi.org/10.1016/j.jmmm.2022.170328

[38] Rostami AK, Hosseinzadeh K, Ganji DD. Hydrothermal analysis of ethylene glycol nanofluid in a porous enclosure with complex snowflake shaped inner wall. Waves Random Complex Media. 2022; 32(1): 1-18. https://doi.org/10.1080/17455030.2020.1758358

[39] Hosseinzadeh K, Roghani S, Mogharrebi AR, Asadi A, Ganji DD. Optimization of hybrid nanoparticles with mixture fluid flow in an octagonal porous medium by effect of radiation and magnetic field. J Therm Anal Calorim. 2021; 143(2): 1413-24. https://doi.org/10.1007/s10973-020-10376-9

[40] Hosseinzadeh K, Montazer E, Shafii MB, Ganji DD. Heat transfer hybrid nanofluid (1-Butanol/MoS2–Fe3O4) through a wavy porous cavity and its optimization. Int J Numer Methods Heat Fluid Flow. 2021; 31(5): 1547-67. https://doi.org/10.1108/HFF-07-2020-0442

[41] Ma Y, Mohebbi R, Rashidi MM, Yang Z, Sheremet MA. Numerical study of MHD nanofluid natural convection in a baffled U-shaped enclosure. Int J Heat Mass Transf. 2019; 130: 123-34. https://doi.org/10.1016/j.ijheatmasstransfer.2018.10.072

[42] Eshaghi S, Izadpanah F, Dogonchi AS, Chamkha AJ, Ben Hamida MB, Alhumade H. The optimum double diffusive natural convection heat transfer in H-shaped cavity with a baffle inside and a corrugated wall. Case Stud Therm Eng. 2021; 28: 101541. https://doi.org/10.1016/j.csite.2021.101541

[43] Nayak MK, Karimi N, Chamkha AJ, Dogonchi AS, El-Sapa S, Galal AM. Efficacy of diverse structures of wavy baffles on heat transfer amplification of double-diffusive natural convection inside a C-shaped enclosure filled with hybrid nanofluid. Sustain Energy Technol Assess. 2022; 52: 102180. https://doi.org/10.1016/j.seta.2022.102180

[44] Li XM, He JD, Tian Y, Hao P, Huang SD. Effects of Prandtl number in quasi-two-dimensional Rayleigh–Bénard convection. J Fluid Mech. 2021; 915: A60. https://doi.org/10.1017/jfm.2021.21

[45] Turkyilmazoglu M. Unsteady convection flow of some nanofluids past a moving vertical flat plate with heat transfer. J Heat Transf. 2014; 136(3): 031704. https://doi.org/10.1115/1.4025730

[46] Rajesh V, Sheremet M. Free convection in a square ternary hybrid nanoliquid chamber with linearly heating adjacent walls. Nanomaterials. 2023; 13(21): 2860. https://doi.org/10.3390/nano13212860

[47] Lizardi A, Terres H, López R, Vaca M, Chávez S, Lara A, Morales JR. Experimental and numerical analysis of convective flow in a square cavity with internal protuberances. J Phys Conf Ser. 2017; 792(1): 012022. https://doi.org/10.1088/1742-6596/792/1/012022

[48] Seo YM, Luo K, Ha MY, Park YG. Direct numerical simulation and artificial neural network modeling of heat transfer characteristics on natural convection with a sinusoidal cylinder in a long rectangular enclosure. Int J Heat Mass Transf. 2020; 152: 119564. https://doi.org/10.1016/j.ijheatmasstransfer.2020.119564

[49] Cho HW, Seo YM, Park YG, Pandey S, Ha MY. Estimation of heat transfer performance on mixed convection in an enclosure with an inner cylinder using an artificial neural network. Case Stud Therm Eng. 2021; 28: 101595. https://doi.org/10.1016/j.csite.2021.101595

[50] Atayılmaz ŞÖ, Demir H, Ağra Ö. Application of artificial neural networks for prediction of natural convection from a heated horizontal cylinder. Int Commun Heat Mass Transf. 2010; 37(1): 68-73. https://doi.org/10.1016/j.icheatmasstransfer.2009.08.009